

Infrared-active phonon modes in monoclinic multiferroic MnWO₄

T. Möller,^{1,2} P. Becker,³ L. Bohatý,³ J. Hemberger,¹ and M. Grüninger¹

¹ II. Physikalisches Institut, Universität zu Köln, Zùlpicher Straße 77, D-50937 Köln, Germany

² I. Physikalisches Institut, Universität zu Köln, Zùlpicher Straße 77, D-50937 Köln, Germany

³ Institut für Kristallographie, Universität zu Köln, Greinstraße 6, D-50939 Köln, Germany

(Dated: June 24, 2014, revised: September 12, 2014)

We report on polarized infrared reflectivity measurements of multiferroic, monoclinic MnWO₄ between 10 K and 295 K. All five non-vanishing components of the dielectric tensor have been determined in the frequency range of the phonons. All infrared-active phonon modes (7 A_u modes and 8 B_u modes) are unambiguously identified. In particular the strongest B_u modes have been overlooked in previous studies, in which the monoclinic symmetry was neglected in the analysis. The combined analysis of reflectance data measured in different experimental geometries (R_{ac} and R_p) is particularly helpful for a proper identification of the B_u modes. Using a generalized Drude-Lorentz model, we determine the temperature dependence of the phonon parameters, including the orientation of the B_u modes within the ac plane. The phonon parameters and their temperature dependence were discussed controversially in previous studies, which did not include a full polarization analysis. Our data do not confirm any of the anomalies reported above 20 K. However, in the paramagnetic phase we find a drastic reduction of the spectral weights of the weakest A_u mode and of the weakest B_u mode with increasing temperature. Below 20 K, the parameters of the A_u phonon modes for $E \parallel b$ show only subtle changes, which demonstrate a finite but weak coupling between lattice dynamics and magnetism in MnWO₄. A quantitative comparison of our infrared data with the quasi-static dielectric constant ϵ_b yields a rough estimate for the oscillator strength $\Delta\epsilon_{\text{em}} \lesssim 0.02$ of a possible electromagnon for $E \parallel b$. Furthermore, we report on a Kramers-Kronig-consistent model which is able to describe non-Lorentzian line shapes in compounds with monoclinic symmetry.

PACS numbers: 63.20.kk, 63.20.-e, 78.30.-j, 77.84.-s

I. INTRODUCTION

The metal tungstate family AWO₄ with divalent A metal ions includes a number of compounds with interesting properties. The range of possible applications is very broad, including (phonon-) scintillation detectors, laser waveguides, laser crystals, and photocatalysis.¹⁻⁶ The compound MnWO₄, also known from nature as mineral *hübnerite*, belongs to the class of multiferroics, displaying a coexistence of antiferromagnetic and ferroelectric order parameters.⁷⁻⁹ The Mn²⁺ ions are in a high-spin 3d⁵ configuration with spin $S = 5/2$. Magnetic frustration leads to a competition of magnetic ground states. Upon cooling, one finds a series of magnetic phase transitions,^{9,10} first to an incommensurate collinear antiferromagnetic phase (AF3) at $T_{N3} = 13.5$ K, then to an incommensurate spiral phase (AF2) at $T_{N2} = 12.5$ K, and finally at $T_{N1} \approx 6.5 - 8.0$ K to a commensurate collinear phase (AF1). A ferroelectric polarization and thus magnetoelectric multiferroicity is observed in the AF2 phase⁷⁻⁹ as well as in a further phase occurring in high magnetic fields.¹¹ The spontaneous polarization is parallel to the b axis.^{8,9} Ferroelectricity originates from the spiral spin structure via the inverse Dzyaloshinskii-Moriya effect.^{7-9,12-14} Recently, it was pointed out that competing isotropic exchange interactions are also important for multiferroicity.¹⁵ The coupling between electric and magnetic effects gives rise to particularly rich physics, ranging from the switching of the electric polarization by an external magnetic field⁷⁻⁹ via the coupling of magnetic and electric domains¹⁶ to second-harmonic generation from

an incommensurate magnetic structure¹⁷ and to a magnetoelectric memory effect.^{18,19}

The magnetoelectric coupling is not restricted to static properties but is also relevant for the dynamics. The character of magnons may change from purely magnetic to magnetoelectric, and these so-called electromagnons can be excited by the electric field component of an electromagnetic wave,²⁰⁻²³ i.e., electromagnons contribute to the optical conductivity and to the dielectric function $\epsilon(\omega)$. The spectral weight of the electromagnons has to be transferred from another dipole-active excitation.^{21,24} In the multiferroic phase of the manganites AMnO₃ (with $A = \text{Gd}_{1-x}\text{Tb}_x$ and $\text{Eu}_{1-x}\text{Y}_x$), the spectral weight of the electromagnons partially stems from the phonon mode lowest in energy.²⁵⁻³³ This behavior differs from the familiar case of proper ferroelectrics with a displacive phase transition. There, the continuous phase transition into the polar phase is accompanied by the softening of an infrared-active phonon mode. At the phase transition, the vanishing phonon frequency ω_0 leads to a divergence of the static permittivity via a diverging contribution to the dielectric function (or oscillator strength) $\Delta\epsilon \propto (\omega_p/\omega_0)^2$, where ω_p denotes the plasma frequency of the phonon. This does not require a change of the phonon's spectral weight $\propto \omega_p^2$ in the optical conductivity. Multiferroic MnWO₄ is an improper ferroelectric, in which ferroelectricity is not directly connected to a softening phonon but rather to the onset of complex magnetic order. In this case, the multiferroic phase transition may be accompanied by the softening of an electromagnon as discussed for DyMnO₃.³⁴ A finite spectral

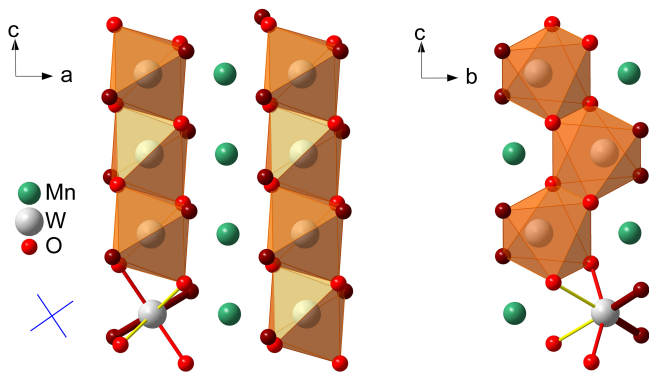


FIG. 1: (Color online) Sketch of the crystal structure of monoclinic MnWO_4 highlighting the chains of WO_6 octahedra running along the c axis. Left: ac plane, right: bc plane. Dark red spheres refer to the $\text{O}(2)$ ions with short $\text{W}-\text{O}(2)$ bonds of only 1.79 Å. The WO_6 octahedra are connected along edges via two $\text{O}(1)$ ions (light red spheres). Within one octahedron, the diagonals are either formed by a short $\text{W}-\text{O}(2)$ bond (thick, dark red lines) in combination with a long $\text{W}-\text{O}(1)$ bond (2.13 Å, thin, yellow lines) or by two of the shorter $\text{W}-\text{O}(1)$ bonds (1.91 Å, thin, light red lines). The two blue lines in the bottom left corner indicate the orientations of the two highest B_u phonon modes as derived from the infrared reflectance data. The orientations of these two modes support the interpretation as $\text{W}-\text{O}$ bond stretching modes.

weight for electromagnons is expected due to the reduced symmetry in the multiferroic phase with an order parameter of magnetoelectric origin. This spectral weight may stem from the phonons.²¹ A detailed study of the lattice vibrations and of the phonon parameters thus may provide valuable information about the ferroelectric transition and the spin-lattice coupling.

In monoclinic MnWO_4 , several results suggest that the spin-lattice coupling is only weak. High-resolution thermal expansion data show subtle but clear anomalies at both T_{N1} and T_{N3} .³⁵ The ferroelectric polarization is of the order of $50 \mu\text{C}/\text{m}^2$,^{8,9} more than an order of magnitude smaller than in, e.g., TbMnO_3 .³⁶ At T_{N1} , the static dielectric constant along the b axis, ϵ_b , shows only a small jump of roughly 0.01,^{8,9} which is about two orders of magnitude smaller than the effects observed in the manganites at low frequencies.³⁶

The phonon modes of MnWO_4 have been studied by Raman scattering and optical spectroscopy. Using polarized Raman scattering, Iliev *et al.*³⁷ found no anomalies of the phonon parameters down to 5 K, while Dura *et al.*³⁸ reported an enhanced damping of several phonon modes in the ferroelectric AF2 phase which was attributed to spin-phonon interactions. In contrast, Hoang *et al.*³⁹ observed phonon anomalies at about 50 K and between 150 and 200 K in their Raman data of MnWO_4 and suggested a new phase transition at 180 K, far above the known magnetic phase-transition temperatures. As far as the infrared-active phonon modes are concerned, a consistent description is still lacking. Choi *et al.*⁴⁰ mea-

sured polarized reflectivity spectra for three different polarization directions of the electric field E ($E \parallel a$, b , and c), which is not sufficient for a proper identification of the eigenmodes in this monoclinic compound where a and c are not mutually perpendicular. To the best of our knowledge, an analysis of the full dielectric tensor in the frequency range of the phonons has not been reported for any monoclinic tungstate AWO_4 with divalent A metal ions thus far. Choi *et al.*⁴⁰ found no anomalies of the phonons as a function of temperature and reported only representative data on the temperature dependence for two high-energy features above 80 meV.

Remarkably, stronger anomalies were reported both in Raman and infrared data for polycrystalline samples of $\text{Mn}_{1-x}\text{A}_x\text{WO}_4$ doped with a few percent of $A = \text{Fe}$, Co , or Ni .^{41,42} Most of these anomalies were observed between 20 K and 200 K, i.e., far above the magnetic phase-transition temperatures of undoped MnWO_4 . In the case of $A = \text{Co}$, high-resolution synchrotron X-ray diffraction data⁴³ for $x = 0.05$ and 0.20 show only small anomalies at the magnetic phase transitions. Moreover, the reported eigenfrequencies of the slightly doped samples^{41,42} strongly deviate from those reported for pure MnWO_4 .⁴⁰ None of these studies takes the monoclinic structure fully into account. For monoclinic symmetry, optical phonon modes in general show a mixture of transverse (TO) and longitudinal (LO) character, and this mixture depends on the direction of the wavevector k . Due to the LO-TO splitting, the eigenfrequency of a given phonon mode also depends on the direction of k , thus the apparent peak frequency varies with the geometry of the experiment.^{44,45} This explains the difficulties in determining the correct eigenfrequencies, in particular for polycrystalline samples.

Further infrared studies were performed on nanocrystalline MnWO_4 with different morphologies of the nanoparticles.⁴⁶⁻⁴⁸ In contrast to Raman modes, the infrared-active phonons show a pronounced dependence on particle size and morphology.^{46,47} As stated above, this is not surprising since the TO-LO mixture and thus the mode frequency depend on the direction of k .⁴⁴ It has been concluded⁴⁶ that a detailed understanding of the bulk modes is a prerequisite for a correct description of the phonon modes of nanocrystals.

Here, we report on a full polarization analysis of single-crystalline MnWO_4 , which allows us to identify unambiguously all expected phonon modes, both for A_u and B_u symmetry. Using a generalized Drude-Lorentz model, we determine the temperature dependence of all phonon parameters, including the orientation of the B_u modes within the ac plane. A comparison to previous studies⁴⁰⁻⁴² shows that in particular the strongest modes have been overlooked thus far. This surprising result can be explained easily. Weaker modes show a small LO-TO splitting and thus give rise to rather narrow but clear features. Strong modes with a very large LO-TO splitting yield broad features, and the orientational dispersion of the dielectric tensor gives rise to unusual line shapes

of these broad peaks. Moreover, the TO-LO mixture depends on the direction of the wavevector k ; thus the eigenfrequency of modes with a large LO-TO splitting may change strongly as a function of k .

The paper is organized as follows. Experimental details are given in Sec. II, followed in Sec. III by a factor-group analysis. Section IV describes the dielectric tensor in monoclinic symmetry as well as the models used to analyze the infrared data, i.e., a generalized Drude-Lorentz model (Sec. IV A), an asymmetric, Kramers-Kronig-consistent oscillator model (Sec. IV B), and a Kramers-Kronig-constrained variational approach (Sec. IV D). The reflectivities R_b , R_{ac} , and R_p measured in different experimental geometries are introduced in Sec. IV C. Section V describes our results for the phonon modes. In Sec. V A and V B we address the A_u and B_u modes, respectively, followed by a detailed discussion of the line shape of the highest B_u mode in Sec. V C. Finally, the temperature dependence and the transfer of spectral weight from the phonons to either lower or higher frequencies are discussed in Sec. V D. Conclusions are given in Sec. VI.

II. EXPERIMENT

Single crystals of MnWO_4 were grown from the melt using the top-seeding technique. The Mn ions can be kept in the divalent state during growth by using a high growth temperature and avoiding melt solvents.⁵ We obtained ruby-red transparent crystals with dimensions up to $5 \times 5 \times 25 \text{ mm}^3$. The crystal structure^{49,50} of MnWO_4 is monoclinic with space group $P2_1/c$, the monoclinic angle amounts to $\beta = 91.08^\circ$. Edge-sharing distorted $[\text{MnO}_6]$ octahedra and edge-sharing distorted $[\text{WO}_6]$ octahedra form alternating zig-zag chains running along the c axis, see Fig. 1. We used natural growth faces and Laue diffraction for the crystallographic sample orientation. After orientation, the samples were lapped and polished.

Using a BRUKER IFS 66v/S Fourier-transform spectrometer, we performed reflectivity measurements at nine different temperatures ranging from 10 K to 295 K in the frequency range of 50 - 7000 cm^{-1} . The sample was mounted on the cold finger of a continuous-flow He cryostat. The angle of incidence α was about 11° , i.e., near-normal incidence. The incident light was linearly polarized, while the polarization state of the reflected light was not analyzed. The temperature of the sample was measured with a thermometer glued on the sample, avoiding direct thermal contact between thermometer and sample holder. We report data down to 20 K for the paramagnetic phase, for 13 K in the AF3 phase, and for 10 K in the multiferroic AF2 phase. The phase transition to the commensurate collinear AF1 phase at 6.5 - 8.0 K could not be reached. Reference measurements were obtained using *in-situ* Au evaporation.

In monoclinic MnWO_4 the b axis is perpendicular to

the ac plane. We use a Cartesian coordinate system with $y \parallel b$, $z \parallel c$, and x lying in the ac plane with $x \perp z$, see Fig. 2b). The reflectivity $R_b(\omega)$ was measured on a surface containing the b axis with polarization of the electric field $E \parallel b$. To avoid any contribution from the ac plane, we chose the (010) plane as plane of incidence, i.e., $R_b(\omega)$ was measured with s -polarized light [$E \perp$ to (010)] with an angle of incidence of $\alpha = 11^\circ$, see Fig. 2a). The sample surface deviates from a (100) surface by 10° , i.e., $\varphi = 80^\circ$ denotes the angle by which the x axis has to be rotated around the y axis to coincide with the sample surface. In the same geometry, we measured the reflectivity $R_p(\omega, \alpha, \varphi)$ for p -polarized light, i.e., with $E \perp b$.

For a full polarization analysis of this monoclinic compound, we measured the reflectivity $R_{ac}(\omega, \chi)$ on a (010) surface, where χ denotes the angle between the incident electric field E and the x axis, see Fig. 2b). For simplicity, we assume normal incidence for the definition of χ and for the analysis of $R_{ac}(\omega, \chi)$. The polarization direction χ was varied by rotating not the sample but the polarizer using a stepper motor. This bears the advantages that the angular precision is higher and that the polarization angle can be changed while the sample is kept at low temperature. The disadvantage is that the incident electric field is not exactly parallel to the ac plane (with the exception of s -polarized light) due to the finite angle of incidence. We measured $R_{ac}(\omega, \chi)$ for $\chi = 0^\circ, 30^\circ, 60^\circ$, and 90° , see Fig. 3. Any three of these data sets can be used to calculate $R_{ac}(\omega, \chi)$ for any value of χ .⁵³ The comparison of the measured reflectivity for $\chi = 60^\circ$ with the calculated one in Fig. 4 demonstrates the consistency of our data.

Additionally, we measured the real part of the quasi-static dielectric constant along the b axis, $\text{Re}\{\varepsilon_b\}$, between 5 K and 50 K at 96.8 kHz and 45 MHz. At 96.8 kHz

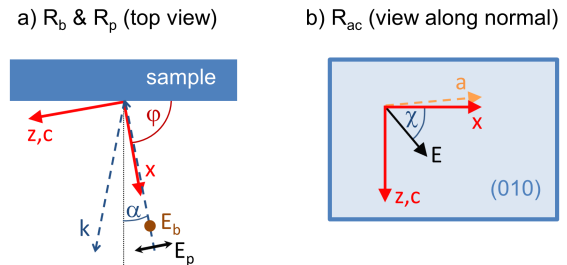


FIG. 2: (Color online) Sketches of the experimental geometries for measuring a) $R_b(\omega)$ and $R_p(\omega, \alpha, \varphi)$ with (010) as plane of incidence, and b) $R_{ac}(\omega, \chi)$ on a (010) surface. In both cases, the view is along the b axis with $b \parallel y$. Red: Cartesian coordinates x and $z \parallel c$. a) Dotted: surface normal. Dashed: wave vectors of incident and reflected light. $\alpha = 11^\circ$ denotes the angle of incidence, and $\varphi = 80^\circ$ is the angle between the x axis and the sample surface. R_b was measured with s -polarized light, R_p with p -polarized light. b) For the analysis of $R_{ac}(\omega, \chi)$ we assume normal incidence. χ denotes the angle by which the polarization direction of the electric field E has to be rotated to coincide with the x axis. The angle $\beta = 91.08^\circ$ between a and c axes is exaggerated for clarity.

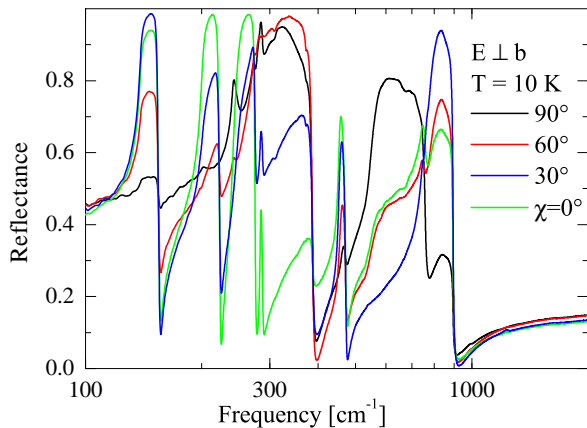


FIG. 3: (Color online) Reflectance $R_{ac}(\omega, \chi)$ of MnWO_4 for $E \perp b$ measured on a (010) surface for four different polarization angles χ at $T = 10$ K, cf. Fig. 2b). Note the logarithmic frequency scale.

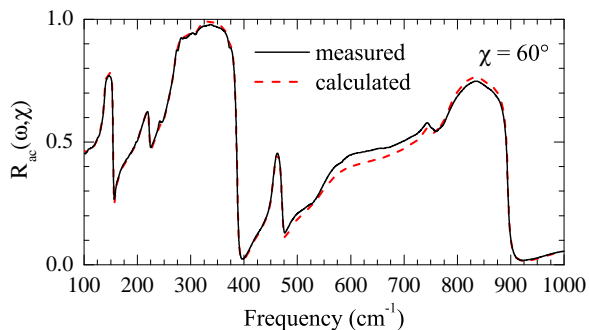


FIG. 4: (Color online) Solid: measured reflectivity $R_{ac}(\omega, \chi)$ for $\chi = 60^\circ$ at $T = 10$ K. Red dashed: calculated reflectivity $R_{ac}^{\text{calc}}(60^\circ) = -\frac{1}{2}R_{ac}(0^\circ) + R_{ac}(30^\circ) + \frac{1}{2}R_{ac}(90^\circ)$. The maximum deviation between measured and calculated data amounts to 5% at about 600 cm^{-1} .

we employed a frequency-response analyzer (NOVOCONTROL) and a small single crystal of MnWO_4 with dimensions of about $2 \times 0.5 \times 2 \text{ mm}^3$ which was prepared as a plate-type capacitor using silver-paint electrodes on the $\{010\}$ surfaces. At 45 MHz we used a micro-strip setup and a vector network analyzer (ROHDE & SCHWARZ). The quasi-static data show a high relative accuracy. Here, we use the results from the infrared data to fix the absolute value of $\text{Re}\{\varepsilon_b\}$.

III. FACTOR-GROUP ANALYSIS

The number of phonon modes can be derived from a factor-group analysis.⁵¹ Monoclinic MnWO_4 with space group $P2/c$ has $Z = 2$ formula units per unit cell. For $T = 295$ K, the site symmetries as well as the irreducible representations of each atomic site are given in Tab. I. In the presence of a center of inversion, Raman activity and infrared activity of normal modes are mutually exclusive.

atom	Wyckhoff notation	site symmetry	irreducible representations
Mn	2(f)	C_2	$A_g + A_u + 2B_g + 2B_u$
W	2(e)	C_2	$A_g + A_u + 2B_g + 2B_u$
O(1)	4(g)	C_1	$3A_g + 3A_u + 3B_g + 3B_u$
O(2)	4(g)	C_1	$3A_g + 3A_u + 3B_g + 3B_u$

TABLE I: Atomic site symmetries⁵ and irreducible representations for the atoms in monoclinic MnWO_4 with space group $P2/c$.

In total the irreducible representations contain 36 modes,

$$\Gamma_{\text{total}} = 8 A_g + 8 A_u + 10 B_g + 10 B_u. \quad (1)$$

Subtracting the acoustic modes ($A_u + 2 B_u$) and the Raman modes ($8 A_g + 10 B_g$), we find 15 infrared-active phonon modes

$$\Gamma_{\text{IR}} = 7 A_u + 8 B_u. \quad (2)$$

The factor-group analysis thus predicts seven A_u modes for polarization of the electric field $E \parallel b$ and eight B_u modes for polarization within the ac plane, $E \perp b$. The magnetic phase transition at T_{N3} is not connected with a structural phase transition,¹⁰ thus our analysis is valid down to $T_{N2} = 12.5$ K. Below T_{N2} , the appearance of ferroelectricity reflects the loss of a mirror plane and a concurrent change of the selection rules. Thus, the distinction between Raman-active and infrared-active modes is not strictly valid anymore. However, the ferroelectric polarization P_b is only small⁷⁻⁹ in MnWO_4 , about $50 \mu\text{C}/\text{m}^2$. Hence the ionic displacements $\delta u \propto P_b$ are expected to be small, and they have escaped detection in structural studies so far.¹⁰ Accordingly, we expect that the Raman-active modes acquire only a tiny oscillator strength $\Delta\varepsilon \propto P_b^2$ in the dielectric function⁵² below T_{N2} , possibly below the detection limit.

IV. DIELECTRIC RESPONSE OF A MONOCLINIC COMPOUND

In monoclinic MnWO_4 , the tensor of the dielectric function $\hat{\varepsilon}(\omega)$ has the following form:

$$\hat{\varepsilon}(\omega) = \begin{pmatrix} \varepsilon_{xx}(\omega) & 0 & \varepsilon_{xz}(\omega) \\ 0 & \varepsilon_{yy}(\omega) & 0 \\ \varepsilon_{xz}(\omega) & 0 & \varepsilon_{zz}(\omega) \end{pmatrix}. \quad (3)$$

Here, we used the Cartesian coordinate system defined in Sec. II with $y \parallel b$, $z \parallel c$, and x lying in the ac plane (see Fig. 3). In the absence of an external magnetic field and neglecting a possible magnetization, the off-diagonal matrix elements ε_{xz} and ε_{zx} are equal. We decompose the three-dimensional tensor $\hat{\varepsilon}(\omega)$ into a scalar $\varepsilon_b(\omega) =$

$\varepsilon_{yy}(\omega)$ and a two-dimensional tensor

$$\hat{\varepsilon}_{ac}(\omega) = \begin{pmatrix} \varepsilon_{xx}(\omega) & \varepsilon_{xz}(\omega) \\ \varepsilon_{xz}(\omega) & \varepsilon_{zz}(\omega) \end{pmatrix}. \quad (4)$$

The scalar $\varepsilon_b(\omega)$ contains information on the A_u modes and can be studied by measuring the reflectivity $R_b(\omega)$ with $E \parallel b$ and a subsequent analysis using a Drude-Lorentz model (see Sec. IV A). For the analysis of $\hat{\varepsilon}_{ac}(\omega)$ and the modes with B_u symmetry, we employed three different methods: a generalized Drude-Lorentz model^{45,53} (see Sec. IV A), an oscillator model which takes an asymmetric (non-Lorentzian) line shape into account (see Sec. IV B), and a Kramers-Kronig-constrained variational analysis⁵⁴ (KKvar, see Sec. IV D). The two-dimensional tensor $\hat{\varepsilon}_{ac}(\omega)$ can be determined by measuring the reflectivity $R_{ac}(\omega, \chi)$ with $E \perp b$ for three different polarization directions χ (see Sec. II and Fig. 2). For the analysis of $R_{ac}(\omega, \chi)$, we assume normal incidence and that only transverse modes are excited by the incident wave. For $E \perp b$, the excitation of purely transverse modes actually requires that $k \parallel b$, i.e., strictly normal incidence on the (010) plane. *A posteriori*, this assumption of purely transverse excitations is validated by our analysis with the exception of the B_u mode highest in energy, which is nearly degenerate with a longitudinal mode and shows a non-Lorentzian line shape (see Sec. V C). We use the terms *transverse mode* and *longitudinal mode* for, e.g., the discussion of a strong Reststrahlen band (with reflectance close to 1) in $R_{ac}(\omega, \chi)$, even though a strict distinction between TO and LO modes is generally not valid for monoclinic symmetry.

A. Generalized Drude-Lorentz model

To determine the scalar $\varepsilon_b(\omega)$ from the measured reflectivity data in the frequency range of the phonon modes, $\varepsilon_b(\omega)$ can be described by a sum of oscillators. We employ a Drude-Lorentz model

$$\varepsilon_b(\omega) = \varepsilon_b^\infty + \sum_{i, A_u} \frac{\omega_{p,i}^2}{\omega_{0,i}^2 - \omega^2 - i\gamma_i\omega}, \quad (5)$$

where ε_b^∞ denotes the high-frequency dielectric constant, $\omega_{0,i}$ the transverse eigenfrequency, $\omega_{p,i}$ the plasma frequency, and γ_i the damping of the i -th oscillator, where i is running over all A_u modes. The oscillator strength is given by $\Delta\varepsilon_i = (\omega_{p,i}/\omega_{0,i})^2$.

The parametrization of $\hat{\varepsilon}_{ac}(\omega)$ is somewhat more difficult because the axes a and c are not mutually perpendicular. For any frequency, one can find a set of orthogonal axes within the ac plane that yields a diagonal form of the real part of $\hat{\varepsilon}_{ac}$ and a second set of axes for which the imaginary part is diagonal. In the case of an orthorhombic crystal, the two sets of axes coincide and are fixed with respect to the crystallographic axes. In the case of monoclinic MnWO_4 , symmetry fixes only the y

axis of the tensor $\hat{\varepsilon}$ with respect to the crystallographic axes, the two other axes may rotate within the ac plane. The rotation angles $\phi_{\text{Re}}(\omega)$ and $\phi_{\text{Im}}(\omega)$ of the principal axes of $\text{Re}\{\hat{\varepsilon}_{ac}(\omega)\}$ and $\text{Im}\{\hat{\varepsilon}_{ac}(\omega)\}$ may differ from each other and depend on the frequency ω . This orientational dispersion of the principal axes of the dielectric tensor usually gives rise to so-called axial dispersion, i.e., an orientational dispersion of the optical axes. For a given frequency ω_0 , $\phi_{\text{Re}}(\omega_0) \neq \phi_{\text{Im}}(\omega_0)$ implies that the complex tensor $\hat{\varepsilon}_{ac}(\omega_0)$ cannot be diagonalized by a rotation. In terms of an oscillator model, the orientational dispersion of $\hat{\varepsilon}_{ac}(\omega)$ can be described by assigning a particular orientation to each oscillator. This generalized Drude-Lorentz (gDL) model^{45,53} reads

$$\hat{\varepsilon}_{ac}^{\text{gDL}}(\omega) = \hat{\varepsilon}_{ac}^\infty + \sum_{i, B_u} \frac{\omega_{p,i}^2}{\omega_{0,i}^2 - \omega^2 - i\gamma_i\omega} \times S(\theta_i) \begin{pmatrix} 1 & 0 \\ 0 & 0 \end{pmatrix} S^{-1}(\theta_i), \quad (6)$$

where $\hat{\varepsilon}_{ac}^\infty$ is a symmetric real two-dimensional tensor denoting the high-frequency contribution, θ_i is the angle by which the dipole moment of mode i has to be rotated to coincide with the x axis, and $S(\theta_i)$ is the rotation matrix

$$S(\theta_i) = \begin{pmatrix} \cos \theta_i & -\sin \theta_i \\ \sin \theta_i & \cos \theta_i \end{pmatrix}. \quad (7)$$

Note that θ_i and $\phi_{\text{Im}}(\omega_{0,i})$ or $\phi_{\text{Re}}(\omega_{0,i})$ do not necessarily coincide. In the case of a weak mode, $\phi_{\text{Im}}(\omega_{0,i})$ may be dominated by a stronger mode which is close in energy, and thus θ_i and $\phi_{\text{Im}}(\omega_{0,i})$ may differ significantly from each other.⁵⁵

B. Asymmetric oscillator model

On the whole, the generalized Drude-Lorentz model yields a satisfactory description of the reflectance of MnWO_4 . However, the highest B_u phonon mode shows an unusual line shape in $R_{ac}(\omega, \chi)$ (see Sec. V C). In the case of a *scalar* dielectric function, an asymmetric line shape [or, more precisely, a non-Lorentzian line shape of $\varepsilon(\omega)$] can be described using a factorized four-parameter model^{41,56,57} which employs two different values $\gamma_{T,i}$ and $\gamma_{L,i}$ for the damping of the i -th oscillator at the transverse and longitudinal eigenfrequencies. This mimics an approximately quadratic frequency dependence of the damping $\gamma = \gamma(\omega)$. However, the condition $\gamma_{L,i} > \gamma_{T,i}$ has to be satisfied,⁵⁸ thus the factorized model is capable of describing an asymmetric mode which is steep at low frequencies and washed out at the high-frequency side. Our data show the opposite behavior (see below). Moreover, the factorized model describes a *scalar* dielectric function and cannot be written as a sum of individual oscillators, thus the generalization of the factorized model

for monoclinic symmetry with orientational dispersion of $\hat{\varepsilon}_{ac}(\omega)$ is not straightforward.

In the case of the tensor $\hat{\varepsilon}_{ac}(\omega)$, we choose a different approach for the description of a non-Lorentzian line shape, starting from a sum of oscillators as described in Eq. 6. A thorough discussion of the frequency dependence of the damping $\gamma(\omega)$ requires to treat $\gamma(\omega)$ as a response function to keep $\hat{\varepsilon}_{ac}(\omega)$ Kramers-Kronig consistent, i.e., to obey causality. To this end, we consider the coupling between two oscillators as discussed by Barker and Hopfield⁵⁹ (a simplified version valid in a narrow frequency range has been proposed by Humlíček *et al.*⁶⁰). More precisely, we study the coupling of one infrared-active mode (IR) and one IR-silent mode (s) with vanishing effective charge to describe the unusual line shape of the highest B_u mode. A possible candidate for the IR-silent mode is a Raman-active mode. In MnWO_4 , we find the highest B_u mode at 767 cm^{-1} at 10 K which is close in energy to the highest B_g mode observed at 776 cm^{-1} at 5 K.³⁷ Another possible origin of the asymmetric line shape is the mixing between transverse and longitudinal modes, see Sec. V C. However, we may also adopt a phenomenological point of view, in which case we do not attempt to assign this silent mode to a particular eigenmode of the compound but view it as a phenomenological source for an asymmetric line shape of the infrared-active mode. The dielectric function can be derived from the classical equations of motion for two damped harmonic oscillators with eigenfrequencies ω_{IR} and ω_s and damping constants γ_{IR} and γ_s , respectively,

$$\begin{aligned}\ddot{x}_{\text{IR}} &= -\omega_{\text{IR}}^2 x_{\text{IR}} - \omega_{\text{IRs}}^2 (x_{\text{IR}} - x_s) - \gamma_{\text{IR}} \dot{x}_{\text{IR}} + \frac{eE_0}{m} e^{-i\omega t} \\ \ddot{x}_s &= -\omega_s^2 x_s - \omega_{\text{IRs}}^2 (x_s - x_{\text{IR}}) - \gamma_s \dot{x}_s\end{aligned}\quad (8)$$

where x_i denotes the displacement of oscillator $i \in \{\text{IR}, s\}$, t is the time, E_0 the amplitude of the driving electric field, e and m are the effective charge and mass of oscillator “IR”, and ω_{IRs} describes the coupling. We are only interested in solutions for the polarization P which oscillate with the frequency ω of the driving force,

$$P = \varepsilon_0 [\varepsilon(\omega) - 1] E_0 e^{-i\omega t} = \frac{N}{V} \cdot e x_{\text{IR}} \quad (9)$$

with N/V being the density, and ε_0 being the vacuum permittivity. Thus the dielectric function reads

$$\varepsilon(\omega) = 1 + \frac{\omega_{p,\text{IR}}^2}{\omega_{\text{IR}}^2 + \omega_{\text{IRs}}^2 - \omega^2 - i\gamma_{\text{IR}}\omega - \frac{\omega_{\text{IRs}}^4}{\omega_s^2 + \omega_{\text{IRs}}^2 - \omega^2 - i\gamma_s\omega}} \quad (10)$$

with the plasma frequency

$$\omega_{p,\text{IR}}^2 = \frac{1}{\varepsilon_0} \frac{N}{V} \frac{e^2}{m}. \quad (11)$$

Equation 10 reduces to the conventional Drude-Lorentz model (cf. Eq. 5) for $\omega_{\text{IRs}} = 0$. For finite ω_{IRs} , the damping is not a real function of ω but is effectively described

by a complex term. The main merit of this model is that it offers a Kramers-Kronig-consistent way for the description of a non-Lorentzian line shape, which requires the introduction of three additional parameters (ω_s , γ_s , and the coupling ω_{IRs}). Here, we use this asymmetric model only for the B_u phonon mode with the highest eigenfrequency. The total dielectric function thus reads

$$\begin{aligned}\hat{\varepsilon}_{ac}^{\text{asym}}(\omega) &= \hat{\varepsilon}_{ac}^{\infty} + \sum_{i=1}^7 \frac{\omega_{p,i}^2}{\omega_{0,i}^2 - \omega^2 - i\gamma_i\omega} \\ &\quad \times S(\theta_i) \begin{pmatrix} 1 & 0 \\ 0 & 0 \end{pmatrix} S^{-1}(\theta_i) \\ &\quad + \frac{\omega_{p,8}^2}{\omega_{0,8}^2 - \omega^2 - i\gamma_8\omega - \frac{\omega_{\text{IRs}}^4}{\omega_{0,s}^2 - \omega^2 - i\gamma_s\omega}} \\ &\quad \times S(\theta_8) \begin{pmatrix} 1 & 0 \\ 0 & 0 \end{pmatrix} S^{-1}(\theta_8),\end{aligned}\quad (12)$$

with the abbreviations $\omega_{0,8}^2 := \omega_{\text{IR}}^2 + \omega_{\text{IRs}}^2$ and $\omega_{0,s}^2 := \omega_s^2 + \omega_{\text{IRs}}^2$.

C. Reflectance and Fitting Procedure

For (near-)normal incidence, the reflectance $R_b(\omega)$ for $E \parallel b$ is given by

$$R_b(\omega) = \left| \frac{1 - \sqrt{\varepsilon_b(\omega)}}{1 + \sqrt{\varepsilon_b(\omega)}} \right|^2. \quad (13)$$

whereas the reflectance $R_{ac}(\omega, \chi)$ is related to the tensor $\hat{\varepsilon}_{ac}(\omega)$ via^{45,53}

$$\begin{aligned}R_{ac}(\omega, \chi) &= \left| \left(\left[\hat{1} - \sqrt{\hat{\varepsilon}_{ac}(\omega)} \right] \cdot \left[\hat{1} + \sqrt{\hat{\varepsilon}_{ac}(\omega)} \right]^{-1} \right) \right. \\ &\quad \left. \times \begin{pmatrix} \cos \chi \\ \sin \chi \end{pmatrix} \right|^2,\end{aligned}\quad (14)$$

where $\hat{1}$ and $(\dots)^{-1}$ denote the unity tensor and the inverse tensor, respectively. The square root of the tensor $\hat{\varepsilon}_{ac}(\omega)$ is taken by rotating $\hat{\varepsilon}_{ac}(\omega)$ to a diagonal form (employing a “rotation” matrix with complex entries), then taking the square root for each matrix element, and the resulting matrix is rotated back to its original basis.^{45,53}

The reflectivity $R_p(\omega, \alpha, \varphi)$ measured for p -polarized light with (010) as plane of incidence [see Sec. II and Fig. 2a)] is given by⁴⁴

$$R_p(\omega, \alpha, \varphi) = \left| \frac{C \cos(\alpha) - \sqrt{\varepsilon_{ww}(\omega) - \sin^2(\alpha)}}{C \cos(\alpha) + \sqrt{\varepsilon_{ww}(\omega) - \sin^2(\alpha)}} \right|^2 \quad (15)$$

$$\text{with } C = \sqrt{\varepsilon_{uu}(\omega)\varepsilon_{ww}(\omega) - \varepsilon_{uw}^2(\omega)}, \quad (16)$$

where $\alpha = 11^\circ$ denotes the angle of incidence. Here, we use a Cartesian coordinate system u, v, w with $v \parallel b$ and w normal to the surface, and φ denotes the angle between the x axis (which is fixed to the crystal axes) and the u axis, i.e., the surface, see Fig. 2a). In our case, $\varphi = 80^\circ$. In the basis u, w , the tensor $\hat{\varepsilon}_{ac}(\omega)$ is given by

$$\begin{pmatrix} \varepsilon_{uu} & \varepsilon_{uw} \\ \varepsilon_{uw} & \varepsilon_{ww} \end{pmatrix} = \hat{\varepsilon}_{ac}^{uw}(\varphi, \omega) = S(\varphi) \hat{\varepsilon}_{ac}(\omega) S^{-1}(\varphi), \quad (17)$$

with the rotation matrix $S(\varphi)$ as described in Eq. 7. For $E \perp b$, the parameters of the generalized Drude-Lorentz model and of the asymmetric oscillator model were obtained by fitting the measured reflectance $R_{ac}(\omega, \chi)$ and $R_p(\omega, \alpha, \varphi)$ simultaneously. In $R_p(\omega, 11^\circ, 80^\circ)$, transverse and longitudinal modes are strongly mixed. The consideration of $R_p(\omega, 11^\circ, 80^\circ)$ thus offers an excellent test for the validity of the analysis, see Sec. V C.

For the fits we employed the MAGIX package (Modeling and Analysis Generic Interface for eXternal numerical codes)⁶¹, which permits us to combine different optimization algorithms to make use of their specific advantages. One may, e.g., combine a swarm algorithm to roughly localize a minimum in parameter space with the Levenberg-Marquardt algorithm to optimize the parameters. Due to the large number of parameters, we typically used only the Levenberg-Marquardt algorithm. However, we employed the particle-swarm-optimization algorithm and the interval-nested-sampling algorithm⁶¹ to search for alternative parameter values of weak oscillators.

D. Kramers-Kronig-constrained variational approach

In the case of a scalar dielectric function such as $\varepsilon_b(\omega)$, a Kramers-Kronig analysis of, e.g., the normal-incidence reflectance $R_b(\omega)$ – with appropriate extrapolations to $\omega = 0$ and ∞ – permits a model-independent determination of $\varepsilon_b(\omega)$. An extension to monoclinic symmetry has been discussed by Kuzmenko *et al.*⁶² Their approach is still based on a Kramers-Kronig analysis of the measured reflectance data [in this case $R_{ac}(\omega, \chi)$] but employs a variational analysis. More recently, a Kramers-Kronig-constrained generalization of the variational approach (KKvar) has been discussed by Kuzmenko.⁵⁴ In short, it uses a large number N of oscillators, where N is comparable to the number of measured data points. The N eigenfrequencies $\omega_1, \dots, \omega_N$ may, e.g., coincide with the frequency points of the measured data. The fixed width of each oscillator is of the order of the step size $\omega_{i+1} - \omega_i$, thus the contribution of any oscillator to the imaginary part $\text{Im}\{\varepsilon^{\text{KKvar}}(\omega)\}$ is restricted to a small frequency interval. The oscillator strengths of the N oscillators are used to parametrize the frequency dependence of $\text{Im}\{\varepsilon^{\text{KKvar}}(\omega)\}$, whereas the real part $\text{Re}\{\varepsilon^{\text{KKvar}}(\omega)\}$

is obtained via a Kramers-Kronig transformation. Finally, the oscillator strengths are varied by fitting the experimental data. Due to the large number of oscillators, this approach is well suited to describe asymmetric non-Lorentzian line shapes of phonon modes or tiny spectral details and still yields a Kramers-Kronig-consistent result for the dielectric function.

Here, we use $3N$ oscillators with a triangular profile⁵⁴ at N frequency points to parametrize $\text{Im}\{\varepsilon_{xx}^{\text{KKvar}}(\omega)\}$, $\text{Im}\{\varepsilon_{xz}^{\text{KKvar}}(\omega)\}$, and $\text{Im}\{\varepsilon_{zz}^{\text{KKvar}}(\omega)\}$. To reduce the calculational effort, we use a step size of 1 cm^{-1} with $\omega_1 = 100 \text{ cm}^{-1}$ and $\omega_N = 1000 \text{ cm}^{-1}$. A Kramers-Kronig analysis requires a reasonable extrapolation beyond the underlying frequency mesh ω_1 to ω_N . Therefore, the result $\hat{\varepsilon}_{ac}^{\text{gDL}}$ of the generalized Drude-Lorentz fit (cf. Eq. 6) is used as a starting point. The total dielectric function reads

$$\hat{\varepsilon}_{ac}^{\text{total}}(\omega) = \hat{\varepsilon}_{ac}^{\text{gDL}}(\omega) + \hat{\varepsilon}_{ac}^{\text{KKvar}}(\omega). \quad (18)$$

The signs of $\text{Im}\{\varepsilon_{xx}^{\text{KKvar}}(\omega)\}$, $\text{Im}\{\varepsilon_{xz}^{\text{KKvar}}(\omega)\}$, and $\text{Im}\{\varepsilon_{zz}^{\text{KKvar}}(\omega)\}$ are arbitrary with the constraints $\text{Im}\{\varepsilon_{xx}^{\text{total}}(\omega)\} \geq 0$ and $\text{Im}\{\varepsilon_{zz}^{\text{total}}(\omega)\} \geq 0$. We use this Kramers-Kronig-constrained variational approach to fit the reflectivity $R_{ac}(\omega, \chi)$ for three different polarization angles ($\chi = 0^\circ, 30^\circ$, and 90°).

V. PHONON MODES

Figures 5 and 6 show the reflectance $R_{ac}(\omega, \chi)$ for three different polarization angles χ as well as $R_p(\omega, \alpha, \varphi)$ and $R_b(\omega)$ at $T = 10 \text{ K}$ and 295 K , respectively. Additionally, we show the reflectance as obtained from the fits based on the generalized Drude-Lorentz model. We fitted $R_p(\omega, \alpha, \varphi)$ and $R_{ac}(\omega, \chi)$ for $\chi \in \{0^\circ, 30^\circ, 90^\circ\}$ simultaneously. The fit parameters are listed in Tab. II. The asymmetric non-Lorentzian line shape observed in $R_{ac}(\omega, \chi)$ in case of the B_u mode highest in energy is discussed in Sec. V C. In Sec. V D, we address the temperature dependence of the spectra which is depicted in Fig. 7 for the low-frequency range.

A. A_u phonon modes

For $E \parallel b$, the agreement between data and fit is excellent, and the analysis is straightforward (see bottom panels of Figs. 5 and 6). The spectra show seven A_u modes, in agreement with the predictions of the factor-group analysis for $T > T_{N2} = 12.5 \text{ K}$. We do not find any additional mode at 10 K , i.e., below T_{N2} . The small discrepancies between data and fit around some of the maxima and minima of $R_b(\omega)$ can be attributed to small deviations from a Lorentzian line shape, typically caused by small contributions stemming from the multi-phonon continuum. Remarkably, the frequency of the highest A_u mode amounts to 859 cm^{-1} , which is unusually high

B_u modes at 10 K/295 K						
ω_0	ω_p	γ	θ	$\Delta\varepsilon$	$\omega_0^{\text{calc}}[41]$	
139/137	310/288	0.7/ 2.6	22/ 20	4.98/4.44	163	
201/197	393/386	1.4/ 5.8	162/157	3.84/3.84	186	
241/239	424/390	0.5/ 1.1	121/122	3.10/2.66	206	
273/277	865/822	2.7/13.2	72/ 72	10.1/8.84	263	
283/283	65/ 45	3.0/ 4.9	168/167	0.05/0.02	323	
455/453	345/319	5.9/14.8	0/ 1	0.58/0.50	467	
554/553	1102/1071	8.3/18.6	123/123	3.96/3.76	576	
767/771	1043/1008	6.6/12.4	34/ 34	1.85/1.71	777	

A_u modes at 10 K/295 K						
ω_0	ω_p	γ	$\Delta\varepsilon$	char.[41]	$\omega_0^{\text{calc}}[41]$	
174/168	348/342	1.1/ 5.4	3.99/4.12	T'	156	
309/306	133/110	2.3/ 4.2	0.18/0.13	$\tau + \delta_{sc}$	246	
341/341	501/494	1.5/ 4.2	2.15/2.11	$\delta_{sc} + \tau$	410	
419/416	308/288	5.2/11.5	0.54/0.48	$\delta_{as} + \tau$	455	
500/498	513/518	9.2/21.0	1.05/1.08	$\nu_{as} + \delta_{sc}$	547	
664/663	756/759	11.5/21.8	1.30/1.31	ν_{as}	671	
859/860	425/422	6.2/10.0	0.24/0.24	ν_s	837	

TABLE II: Parameters of the generalized Drude-Lorentz model for $T=10$ K and 295 K. Here, $\Delta\varepsilon = (\omega_p/\omega_0)^2$ denotes the oscillator strength. The parameters ω_0 , ω_p , and γ are given in units of $[\text{cm}^{-1}]$, whereas the angle θ is given in $[\circ]$. For the high-frequency dielectric constant at $T=10$ K (295 K) we find $\varepsilon_{xx}^\infty = 5.59$ (5.25), $\varepsilon_{yy}^\infty = 5.48$ (5.35), $\varepsilon_{zz}^\infty = 6.25$ (5.88), and $\varepsilon_{xz}^\infty = 0.29$ (0.25). The calculated values for ω_0 (right column) and the characters of the A_u modes are reproduced from Ref. [41], where T' stands for T'(Mn)+T'(W) and denotes a lattice translational mode, τ is a W-O(2) twisting mode, δ_{sc} a W-O(2) scissoring mode, δ_{as} an antisymmetric W-O(1) bending mode, and ν_{as} [ν_s] an antisymmetric W-O(1) [symmetric W-O(2)] stretching mode.⁴¹

for a transition-metal oxide in which oxygen is the only light element. However, comparable values have been reported for other tungstates AWO_4 with divalent $A = \text{Cd}$, Ni , or Mg .^{63–67} This mode can be assigned to a symmetric W-O(2) bond stretching phonon. The high frequency reflects the strong bonding between the nominally hexavalent W ions and the O(2) ions, as the shortest W-O(2) bond in MnWO_4 amounts to only 1.79 Å (see Fig. 1).⁵⁰ Similar energies of stretching modes have been observed in, e.g., multiferroic $\text{Ni}_3\text{V}_2\text{O}_8$ and α' - NaV_2O_5 with nominally penta- and tetravalent V ions.^{24,68} The character of the other A_u modes is given in Tab. II.

As far as the eigenfrequencies $\omega_{0,i}$ of the A_u modes along the unique b axis are concerned, the results of Refs. [40,41] and our data agree very well with each other. With the exception of the lowest A_u mode, the values for $\omega_{0,i}$ agree within about 1-2%. In MnWO_4 , we and Choi *et al.*⁴⁰ found the lowest mode at 168 cm^{-1} at room temperature, whereas it was reported at 180 and 182 cm^{-1} in $\text{Mn}_{0.85}\text{Co}_{0.15}\text{WO}_4$ and $\text{Mn}_{0.97}\text{Fe}_{0.03}\text{WO}_4$, respectively.⁴¹

Note that the values of the damping γ_i and the oscillator strength $\Delta\varepsilon_i$ are not reported for the single-crystal data in Refs. [40,41].

The A_u phonon parameters enable us to determine the contribution $\text{Re}\{\varepsilon_b^{\text{high}}\} = \varepsilon_{yy}^\infty + \sum_{i=1}^7 \Delta\varepsilon_i$ of phonons and of excitations at higher energies to the quasi-static dielectric constant $\text{Re}\{\varepsilon_b\}$, i.e., for frequencies well below the phonon range. Combining this result with low-frequency data measured at 96.8 kHz and 45 MHz – far below the frequency range of a possible electromagnon – allows us to estimate the contribution of a possible electromagnon to $\text{Re}\{\varepsilon_b\}$, which will be discussed together with the temperature dependence in Sec. VD. At 10 K we find $\text{Re}\{\varepsilon_b^{\text{high}}\} = 14.9$. This has to be compared to the results reported from impedance measurements using LCR meters, $\text{Re}\{\varepsilon_b\} = 16.4$ at 1 MHz (Ref. 9) and 12.3 at 1 kHz (Ref. 8). Note that impedance measurements typically show a high relative accuracy but larger errors concerning the absolute value due to uncertainties in the size and shape of the electrodes.

B. B_u phonon modes

The case of $E \perp b$ requires a more careful analysis. The interplay of partially overlapping modes with different rotation angles θ_i gives rise to complex line shapes in $R_{ac}(\omega, \chi)$,⁶⁹ see Figs. 5 – 7. Therefore it is more difficult to disentangle the contributions of the different modes. We find that the data can be described by a sum of eight B_u modes, as predicted by the factor-group analysis for $T > 12.5$ K (cf. Eq. 2). Eight separate B_u modes are most easily recognizable in the data of $R_p(\omega)$. However, the eigenfrequencies can be inferred more easily from $R_{ac}(\omega, \chi)$. Five of the eight B_u modes have an eigenfrequency lower than 300 cm^{-1} , see Tab. II. Four out of these five modes are easily recognized in the spectrum of $R_{ac}(\omega)$ for $\chi = 0^\circ$ below 300 cm^{-1} at $T = 10$ K (see Fig. 7). These four modes have eigenfrequencies of $\omega_{0,1} = 139 \text{ cm}^{-1}$, $\omega_{0,2} = 201 \text{ cm}^{-1}$, $\omega_{0,3} = 241 \text{ cm}^{-1}$, and $\omega_{0,5} = 283 \text{ cm}^{-1}$. The mode with $\omega_{0,4} = 273 \text{ cm}^{-1}$ has a much larger oscillator strength, giving rise to the pronounced Reststrahlen band observed between about 250 cm^{-1} and 400 cm^{-1} for $\chi = 90^\circ$. The eigenfrequency $\omega_{0,4} = 273 \text{ cm}^{-1}$ corresponds to the low-frequency edge of the Reststrahlen band, whereas the steep drop of $R_{ac}(\omega, 90^\circ)$ at about 390 cm^{-1} can be identified with its longitudinal eigenfrequency (see Secs. IV and VC for a discussion of the mixing of LO and TO modes). This mode with $\theta_4 = 72^\circ$ gives rise to the peculiar feature peaking at about 375 cm^{-1} for $\chi = 0^\circ$ and 30° . The sixth mode at $\omega_{0,6} = 455 \text{ cm}^{-1}$ is well separated in frequency from all other modes and thus can be observed easily for all values of χ considered here. Due to the strong orientational dispersion of $\hat{\varepsilon}_{ac}(\omega)$ in the vicinity of this mode (see below), it also affects $R_{ac}(\omega, 90^\circ)$ although $\chi = 90^\circ$ is almost orthogonal to its orientation $\theta_6 \approx 0^\circ$.

Modes number seven and eight determine $R_{ac}(\omega)$ be-

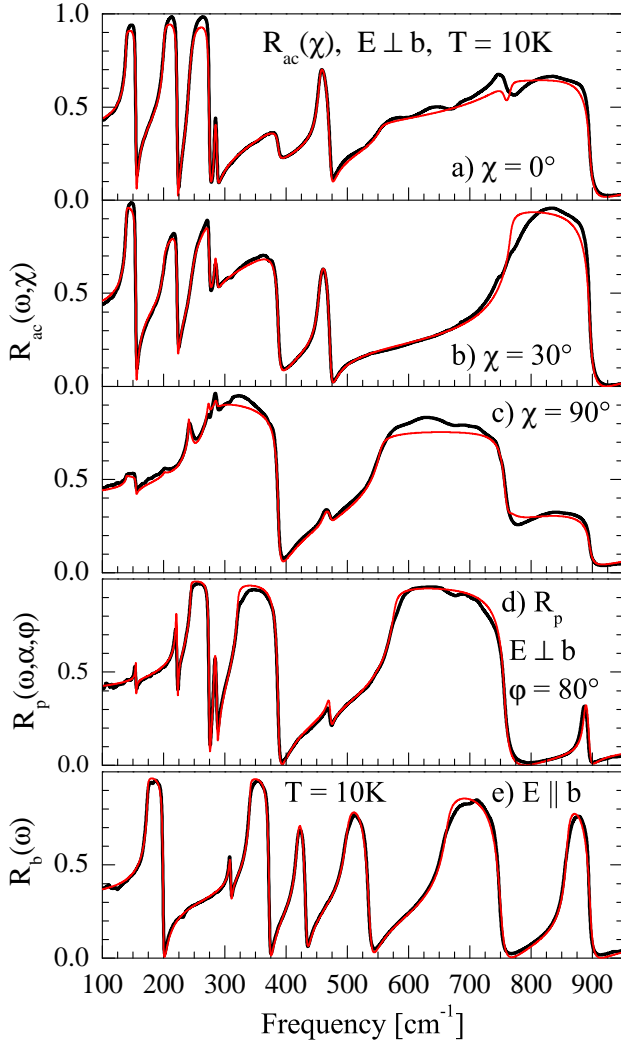


FIG. 5: (Color online) Reflectance of MnWO_4 at $T=10\text{K}$ (black) and generalized Drude-Lorentz fit (red). a) -c) $R_{ac}(\omega, \chi)$ for different polarization angles χ as defined in Fig. 3. d) Reflectance $R_p(\omega, 11^\circ, 80^\circ)$ for p -polarized light incident within the (010) plane with $E \perp b$, see Fig. 2a) and Eq. 15. e) Reflectance $R_b(\omega)$ for $E \parallel b$.

tween 500 and 900cm^{-1} . With $\theta_7 = 123^\circ$ and $\theta_8 = 34^\circ$, these two modes are nearly orthogonal to each other. Accordingly, $R_{ac}(\omega, 30^\circ)$ predominantly shows the higher mode with $\omega_{0,8} = 767\text{cm}^{-1}$. The signature of the lower mode will be most pronounced for $\chi \approx \theta_7 = 123^\circ$, whereas the measured data sets with $\chi = 0^\circ, 60^\circ$, and 90° show complicated line shapes which reflect the existence of both modes. Note that the pronounced peak at about 750cm^{-1} for $\chi = 0^\circ$ does not require to invoke a further infrared-active mode. This peak is located at the frequency of the steep drop of $R_{ac}(\omega, 90^\circ)$, i.e., at the longitudinal eigenfrequency of mode seven with $\omega_{0,7} = 554\text{cm}^{-1}$ (see also Fig. 3). For comparison, it is instructive to consider the nearly triangular hump around 375cm^{-1} for $\chi = 0^\circ$ which stems from the phonon

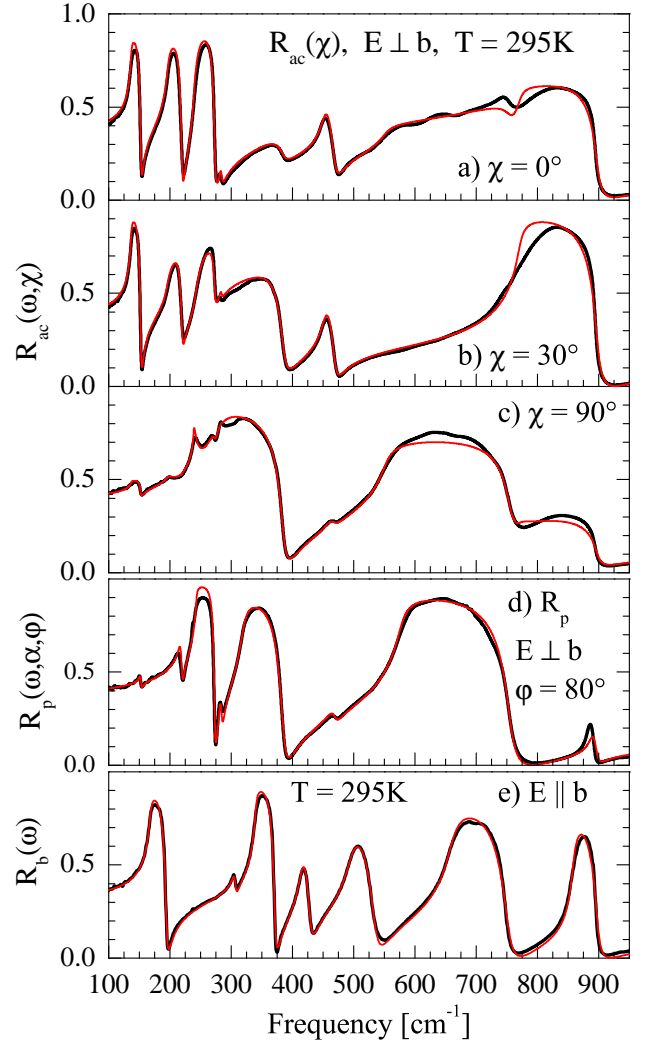


FIG. 6: (Color online) Reflectance of MnWO_4 at $T=295\text{K}$ (black) and generalized Drude-Lorentz fit (red). a) -c) $R_{ac}(\omega, \chi)$ for different polarization angles χ , d) $R_p(\omega, 11^\circ, 80^\circ)$, e) $R_b(\omega)$.

mode with $\theta_4 = 72^\circ$. Similarly, the peculiar shape of the peak at 750cm^{-1} for $\chi = 0^\circ$ or 60° (see Figs. 3 and 4) originates from the phonon mode with $\theta_7 = 123^\circ$, i.e., roughly $\pm 60^\circ$ different from the value of χ . Moreover, lattice dynamical calculations⁴¹ for MnWO_4 predict only two B_u modes above 500cm^{-1} , namely at 576cm^{-1} and 777cm^{-1} , in reasonable agreement with our experimental values of 554cm^{-1} and 767cm^{-1} . Also first-principles calculations⁶⁵ for NiWO_4 find only two modes with B_u symmetry above 500cm^{-1} .

The existence of eight B_u modes is corroborated by the data for $R_p(\omega, \alpha, \varphi)$ measured with p -polarized light and (010) as plane of incidence [see panels (d) of Figs. 5 and 6 and Eq. 15]. In particular, R_p shows the five lowest modes clearly separated from each other and only two B_u modes above 500cm^{-1} . For this measurement geometry, the modes show a strong LO-TO mixing, and

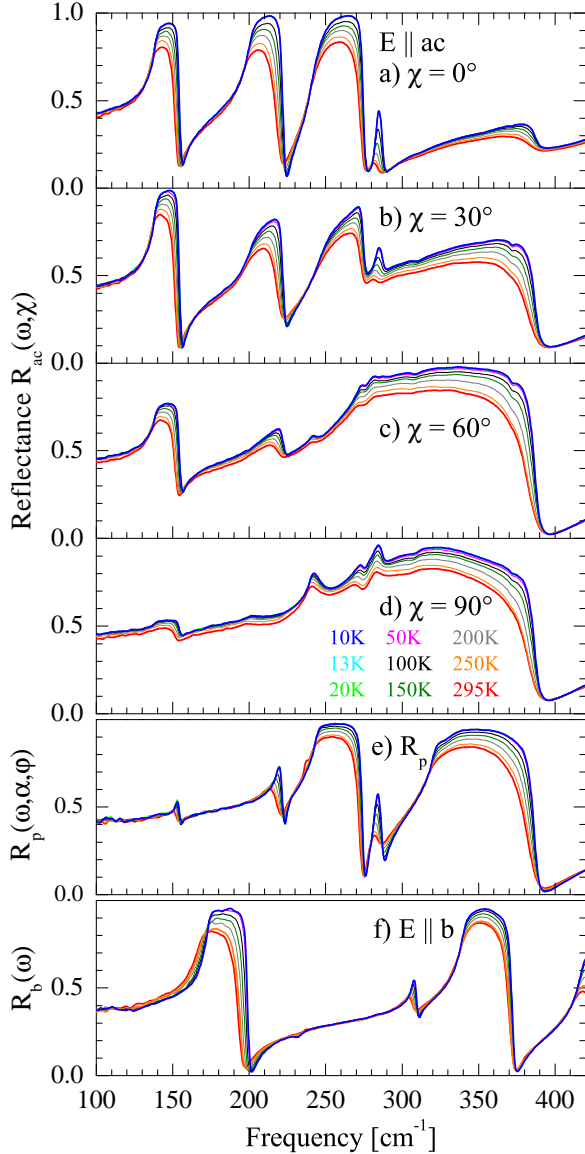


FIG. 7: (Color online) Temperature dependence of the reflectance in the low-frequency range. Panels a)-d): $R_{ac}(\omega, \chi)$, e) $R_p(\omega, 11^\circ, 80^\circ)$, f) $R_b(\omega)$. The largest changes of the spectral weight are observed for the weak B_u mode at 283 cm^{-1} and for the weak A_u mode at 309 cm^{-1} . The lowest A_u mode shows the largest softening.

the character changes from predominantly transverse to predominantly longitudinal as a function of the orientation angle θ_i of the mode with respect to the wave vector k . Accordingly, both the apparent peak position and the oscillator strength depend strongly on the angle of incidence α and on the angle φ , which describes the orientation of the ac plane with respect to the surface [see Fig. 2a) and Eq. 15]. This explains in particular the pronounced changes between $R_{ac}(\omega)$ and $R_p(\omega)$ observed for modes 4 and 8: $R_p(\omega, 11^\circ, 80^\circ)$ shows the high-frequency edges of the phonon modes (i.e., the LO frequencies) at the same frequencies as $R_{ac}(\omega, \chi)$, but the apparent os-

illator strength is very different in R_p and R_{ac} . As a result, all eight B_u modes are clearly separated from each other in R_p , but the apparent order of modes 4 and 5 is reversed. The weak mode 5 gives rise to a feature close to $\omega_{0,5} = 283 \text{ cm}^{-1}$ also in R_p , but the much stronger mode 4 with $\omega_{0,4} = 273 \text{ cm}^{-1}$ appears as a band between 300 cm^{-1} and 400 cm^{-1} in R_p . With small exceptions, our fit describes both $R_p(\omega, \alpha, \varphi)$ and $R_{ac}(\omega, \chi)$ very well. This clearly demonstrates that $\hat{\epsilon}_{ac}(\omega)$ has been determined correctly (cf. Sec. V C).

A Kramers-Kronig-constrained variational analysis of $R_{ac}(\omega, \chi)$ for $\chi \in \{0^\circ, 30^\circ, 90^\circ\}$ (see Sec. IV D) supports our results from the generalized Drude-Lorentz model for the number of modes and for the properties of the lower seven modes. Figure 8 compares $\text{Im}\{\epsilon_{xx}(\omega)\} + \text{Im}\{\epsilon_{zz}(\omega)\}$ obtained by the two approaches. The Kramers-Kronig-constrained variational analysis equally shows four strong B_u modes below 300 cm^{-1} , a weak feature that corresponds to the mode at $\omega_{0,5} = 283 \text{ cm}^{-1}$ (see insets of Figs. 8 and 9), one mode at about 450 cm^{-1} , and two modes above 500 cm^{-1} . The Kramers-Kronig-constrained variational analysis employs a fixed line width and thus encounters problems to precisely describe the phonon modes number 1 and 3 with line widths smaller than 1 cm^{-1} . This explains the spike observed at about 154 cm^{-1} in Fig. 8.

The results of the two approaches for the diagonalized form of the real part of the dielectric function $\text{Re}\{\hat{\epsilon}_{ac}\}$ are given in Fig. 9 for the high-frequency range. The main discrepancy between the generalized Drude-Lorentz model and the Kramers-Kronig-constrained variational approach is observed for the line shape of the highest B_u mode (see Sec. V C).

The rotation angles $\phi_{\text{Im}}(\omega)$, $\phi_{\text{Re}}(\omega)$, and the angles θ_i of the different oscillators of the generalized Drude-Lorentz model are plotted in Fig. 10. Below 500 cm^{-1} , MnWO_4 shows a pronounced orientational dispersion of $\hat{\epsilon}_{ac}(\omega)$. The two high-energy modes above 500 cm^{-1} originate from stretching/bending vibrations of W-O bonds of the tightly bound WO_6 octahedra. Remarkably, the rotation angles $\theta_7 = 123^\circ$ and $\theta_8 = 34^\circ$ of these two modes agree very well with the projections of the W-O bonds on the ac plane, see Fig. 1. The O(2)-O(2) edge of the WO_6 octahedra is rotated by about 30° with respect to the x axis, and the rotation of the shorter O(1)-W-O(1) bond (light red bonds in Fig. 1) amounts to about 123° .

In total, we have identified both the seven A_u modes and the eight B_u modes predicted by a factor-group analysis. This has been claimed before both by Choi *et al.*⁴⁰ and by Maczka *et al.*,⁴¹ but both studies investigated only two polarization directions within the ac plane. Our analysis demonstrates that this is clearly not sufficient to determine the modes with B_u symmetry in this monoclinic compound. In the analysis of the single-crystal data of Maczka *et al.*,⁴¹ modes are missing at 273 cm^{-1} , 283 cm^{-1} , and 554 cm^{-1} in $\text{Mn}_{0.85}\text{Co}_{0.15}\text{WO}_4$ and at 201 cm^{-1} , 273 cm^{-1} , and 455 cm^{-1} in $\text{Mn}_{0.97}\text{Fe}_{0.03}\text{WO}_4$. Partially, these modes have been observed in the poly-

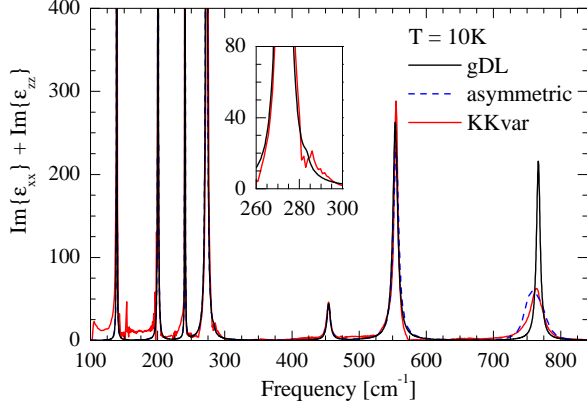


FIG. 8: (Color online) The sum $\text{Im}\{\varepsilon_{xx}(\omega)\} + \text{Im}\{\varepsilon_{zz}(\omega)\}$ shows all eight B_u phonon modes. A Kramers-Kronig-constrained variational analysis of $R_{ac}(\omega, \chi)$ (KKvar, red line, cf. Sec. IV D) confirms the results of a generalized Drude-Lorentz fit (gDL, black line, cf. Eq. 6) with the exception of the line shape of the highest mode at 767 cm^{-1} . For this mode, the KKvar result supports a non-Lorentzian line shape as described by the asymmetric oscillator model (blue dashed line, cf. Eq. 12). Inset: weak mode at 283 cm^{-1} on an enlarged scale.

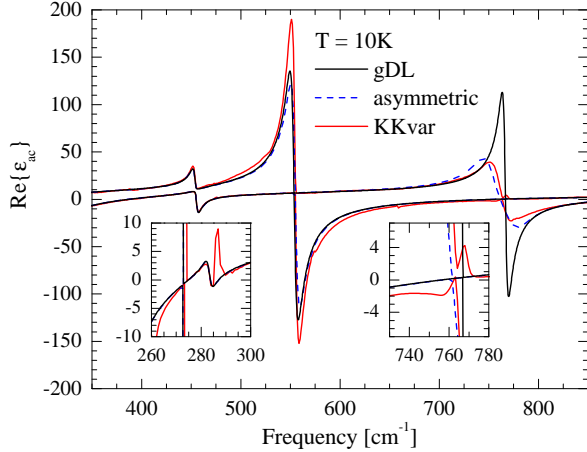


FIG. 9: (Color online) The two entries of the diagonal form of the real part $\text{Re}\{\hat{\varepsilon}_{ac}(\omega, \chi)\}$ at 10 K as obtained from a generalized Drude-Lorentz fit (gDL, black lines, cf. Eq. 6), a Kramers-Kronig-constrained variational analysis of $R_{ac}(\omega, \chi)$ (KKvar, red lines, cf. Sec. IV D), and a fit using an asymmetric, non-Lorentzian line shape for the highest B_u mode (blue dashed lines, cf. Eq. 12). Insets: same data on an enlarged scale.

crystalline samples.⁴¹ Choi et al.⁴⁰ reported 8 frequencies for $E \parallel a$ and 6 more frequencies for $E \parallel c$, 5 (4) of them nearly degenerate with the ones reported for $E \parallel a$ (b). Our data reveal that several of these modes are actually A_u modes, whereas the B_u modes at 273 cm^{-1} , 283 cm^{-1} , 554 cm^{-1} , and 767 cm^{-1} are missing. At first sight, it may seem surprising that in particular the modes with large oscillator strength at 273 cm^{-1} and at 554 cm^{-1}

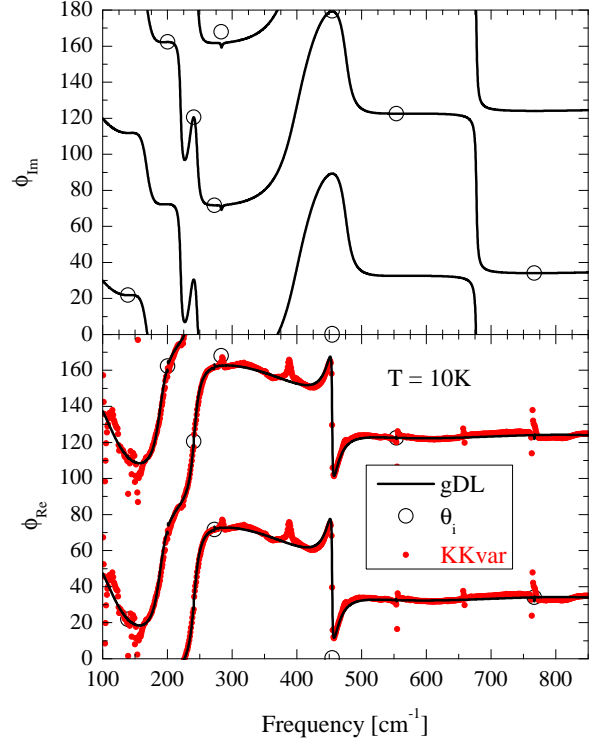


FIG. 10: The rotation angles $\phi_{\text{Im}}(\omega)$ of $\text{Im}\{\hat{\varepsilon}_{ac}(\omega, \chi)\}$ (solid lines, top panel) and $\phi_{\text{Re}}(\omega)$ of $\text{Re}\{\hat{\varepsilon}_{ac}(\omega, \chi)\}$ (solid lines, bottom panel) at 10 K as obtained from a generalized Drude-Lorentz fit (gDL, cf. Eq. 6). Full red symbols: $\phi_{\text{Re}}(\omega)$ as obtained from a Kramers-Kronig-constrained variational analysis. The angles $\phi_{\text{Im}}(\omega)$ and $\phi_{\text{Re}}(\omega)$ are plotted modulo 90° . Open symbols: The angle θ_i between the dipole moment of mode i and the x axis (cf. Tab. II).

have been overlooked. However, our reflectivity data show that in particular the line shapes of the strong modes with large LO-TO splitting – giving rise to spectral overlap with other bands⁶⁹ – depend strongly on the angle χ . Moreover, the reflectivity spectrum of the B_u modes strongly depends on the measurement geometry, i.e., on the direction of the wavevector. Weaker modes give rise to sharper features, which facilitates the determination of their eigenfrequencies.

C. Line shape of the highest B_u mode

The line shape of $R_{ac}(\omega, \chi)$ is not described very well between about 700 cm^{-1} and 800 cm^{-1} if we stick to eight modes with a Lorentzian line shape (see Fig. 11). We emphasize that adding a further Lorentzian mode to $\hat{\varepsilon}_{ac}^{\text{gDL}}(\omega)$ in Eq. 6 does not significantly improve the quality of the fit. The steep drop of the Reststrahlen band at about 900 cm^{-1} indicates a small value of the damping γ_8 of the eighth B_u mode, whereas the much more gradual rise at the low-frequency side of this mode between 700 cm^{-1} and 800 cm^{-1} for $\chi = 30^\circ \approx \theta_8$ is a clear

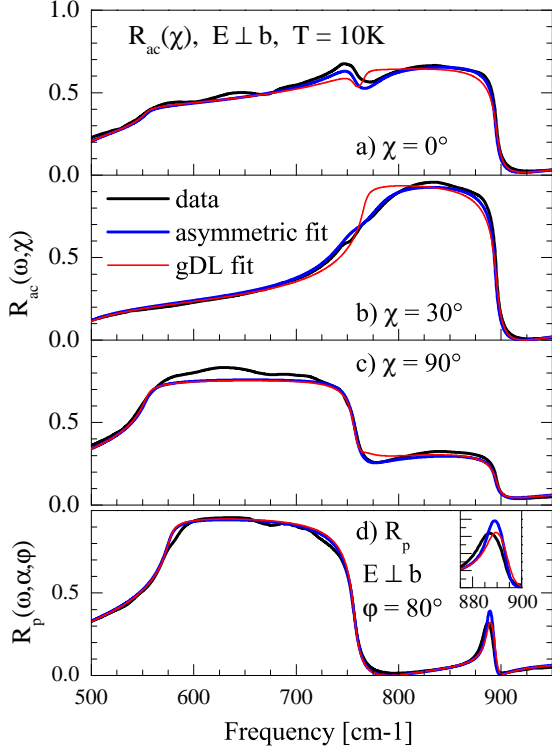


FIG. 11: (Color online) Comparison of fits based on the generalized Drude-Lorentz model (red, cf. Eq. 6) and the asymmetric oscillator model (blue, cf. Eq. 12). In both cases, $R_p(\omega)$ and $R_{ac}(\omega, \chi)$ with $\chi \in \{0^\circ, 30^\circ, 90^\circ\}$ were fitted simultaneously. Black: measured reflectance data. Inset: highest B_u mode on an enlarged scale.

$\omega_{0,8}$	$\omega_{p,8}$	γ_8	θ_8	$\omega_{0,s}$	γ_s	ω_{IRs}
762	1048	3.9	33	765	162	56

TABLE III: Parameters of the asymmetric oscillator model for the eighth B_u mode at $T=10$ K.

signature of a larger damping. Accordingly, a fit based on Eq. 12 with an asymmetric line shape for the mode with $\omega_{0,8} = 767 \text{ cm}^{-1}$ yields a much better description of $R_{ac}(\omega, \chi)$ (cf. blue lines in Fig. 11). The fit parameters are given in Table III. An asymmetric line shape is supported by the Kramers-Kronig-consistent variational analysis of $R_{ac}(\omega, \chi)$ (see Figs. 8 and 9).

In contrast to $R_{ac}(\omega, \chi)$, $R_p(\omega)$ is described very well by the generalized Drude-Lorentz model [red line in panel d) of Fig. 11]. In fact, the description of the highest B_u mode in $R_p(\omega)$ becomes slightly worse if we use the asymmetric oscillator model, which overestimates the absolute value of $R_p(\omega)$ at the maximum of the highest mode at about 880 cm^{-1} . This is a compromise of the fit which aims at a simultaneous description of $R_{ac}(\omega, \chi)$ and $R_p(\omega)$. Note that the agreement between $R_{ac}(\omega, \chi)$ and the fit is not improved significantly if we fit only $R_{ac}(\omega, \chi)$ but not $R_p(\omega)$.

One possible source for the asymmetric line shape

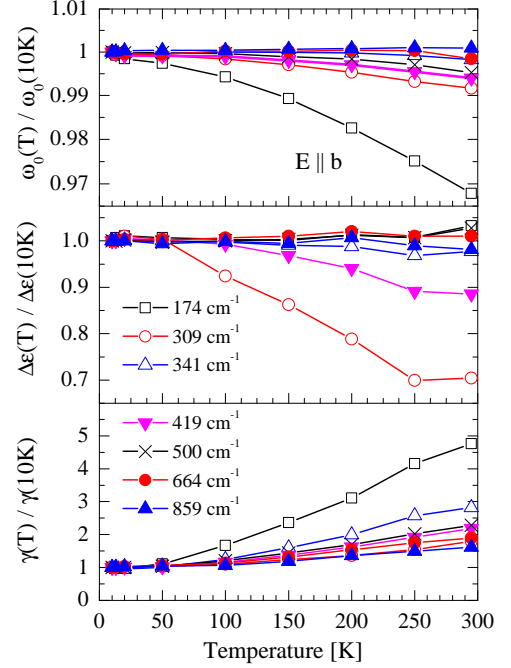


FIG. 12: (Color online) Temperature dependence of the parameters of the Drude-Lorentz fit for $E \parallel b$, i.e., for the A_u phonon modes: eigenfrequency $\omega_{0,i}$, oscillator strength $\Delta\epsilon_i$, and damping γ_i .

in $R_{ac}(\omega, \chi)$ is a mixing of transverse and longitudinal modes. Our analysis of $R_{ac}(\omega, \chi)$ assumes that only transverse modes are excited, which strictly is valid only for normal incidence. This assumption thus may break down for an angle of incidence of $\alpha = 11^\circ$. In the analysis of $R_p(\omega, \alpha, \varphi)$, the finite value of α and the mixing of longitudinal and transverse modes are taken into account, see Eq. 15. The mixing of transverse and longitudinal character is particularly strong if the corresponding eigenfrequencies are nearly degenerate. The near degeneracy of $\omega_{LO,7}$ and $\omega_{0,8}$ is apparent from Fig. 9, which shows the two entries of the diagonal form of the real part $\text{Re}\{\hat{\epsilon}_{ac}(\omega)\}$. The two zero crossings of the diagonal components which correspond to $\omega_{LO,7}$ and $\omega_{0,8}$ nearly coincide in frequency at roughly $760 \text{ cm}^{-1} - 770 \text{ cm}^{-1}$. This is the frequency range with the largest deviations between $R_{ac}(\omega, \chi)$ and the Lorentzian fit. In this range, $\text{Re}\{\hat{\epsilon}_{ac}(\omega)\}$ is close to zero in any direction within the ac plane. We propose that this causes the unusual line shape.

In $R_p(\omega, \alpha, \varphi)$ with $\varphi = 80^\circ$, the highest B_u mode predominantly shows longitudinal character, giving rise to only a small peak close to $\omega_{LO,8}$. The eigenfrequency of this predominantly longitudinal mode does not coincide with $\omega_{LO,7}$, thus the mixing of B_u modes 7 and 8 does not play a role for this geometry. Accordingly, $R_p(\omega, 11^\circ, 80^\circ)$ is well described by a model employing a constant value of γ_8 .

D. Temperature dependence

1. A_u modes

The Drude-Lorentz fit parameters of all A_u phonon modes are plotted as a function of temperature in Fig. 12. Above 20 K, all parameters evolve smoothly with temperature, there is no evidence for any strong anomaly. Six of the seven A_u modes soften by only 1% or less between 10 K and 295 K. The lowest A_u mode with $\omega_{0,1} = 174 \text{ cm}^{-1}$ forms an exception. Between 10 K and 295 K, it softens by 5.6 cm^{-1} or 3%, showing the largest redshift for $E \parallel b$ both on a relative and on an absolute scale. This pronounced shift can be clearly seen in the reflectivity data, see Fig. 7. In Raman data, the largest relative shift of 2.5% between 5 K and 300 K is observed for the lowest A_g mode.³⁷ Also in the case of the B_u modes, the largest relative redshift is observed for the two lowest modes (see below). The phonon softening observed above 20 K can be attributed to the typical thermal expansion of the lattice, reflecting anharmonicity. The damping constants γ_i of all A_u modes behave as expected, showing a smooth increase with increasing temperature. Again, the strongest change (on a relative scale) is observed for the lowest A_u mode. The oscillator strength $\Delta\varepsilon_i$, i.e., the contribution of a given mode i to the real part of ε_b at sub-phonon frequencies, is obtained via $\Delta\varepsilon_i = (\omega_{p,i}/\omega_{0,i})^2$. On a relative scale, the A_u mode at 309 cm^{-1} shows the most pronounced reduction of $\Delta\varepsilon_i$ with increasing temperature, but this mode also has the smallest absolute value of $\Delta\varepsilon_i$ (see Tab. II and Fig. 7). According to Maczka *et al.*,⁴¹ this mode corresponds to a WO_2 bending mode (twisting and scissoring, see Tab. II). Note that the observed phonon softening with increasing temperature leads to an *enhanced* oscillator strength $\Delta\varepsilon_i$. A *decrease* of $\Delta\varepsilon_i$ with increasing temperature reflects that the increase of $1/\omega_{0,i}^2$ is overcompensated by a reduction of the spectral weight $\propto \omega_{p,i}^2$, i.e., of the effective ionic charge.

Below 20 K, we observe only small changes of the phonon parameters of the A_u modes. We focus on the mode with $\omega_{0,1}(10 \text{ K}) = 174 \text{ cm}^{-1}$, which exhibits the largest changes of $\omega_{0,i}$, $\omega_{p,i}$, and $\Delta\varepsilon_i$ at low temperatures. Figure 13 shows the temperature dependence of $\omega_{0,1}$, $\omega_{p,1}^2$, and of $\Delta\varepsilon_1$ on an enlarged scale. The changes of $\omega_{0,1}$ between the different phases amount to only $0.1 - 0.2 \text{ cm}^{-1}$ or 0.1%, which is hard to resolve experimentally. However, the values for $\omega_{0,1}$ found at 10 K and 13 K clearly deviate from the approximately quadratic temperature dependence of $\omega_{0,1}$ observed above 20 K. In particular, the hardening of $\omega_{0,1}$ with decreasing temperature is the opposite of the conventional phonon mode softening occurring in proper ferroelectrics. At the same time, spin-phonon coupling is expected to cause a phonon shift proportional to the nearest-neighbor spin-spin correlation function.⁷⁰⁻⁷⁴ For the spectral weight we find a reduction of $\Delta\omega_{p,1}^2 = [\omega_{p,1}(13 \text{ K})]^2 - [\omega_{p,1}(10 \text{ K})]^2 \approx$

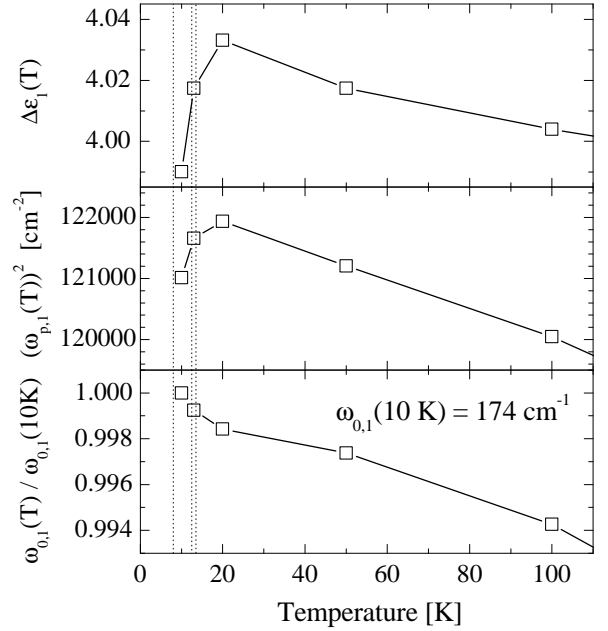


FIG. 13: (Color online) Eigenfrequency $\omega_{0,1}$ (bottom), spectral weight $\propto \omega_{p,1}^2$ (middle), and oscillator strength $\Delta\varepsilon_1$ of the lowest A_u phonon mode. Dotted lines: phase transition temperatures.

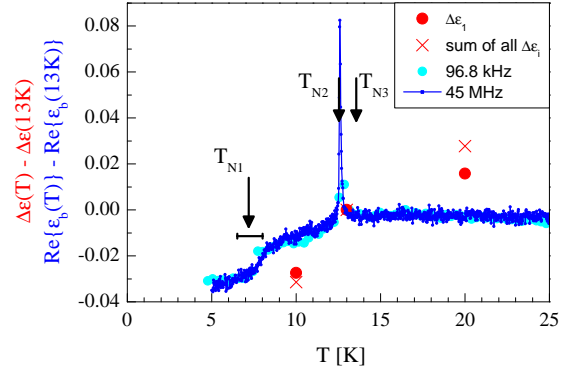


FIG. 14: (Color online) Blue and cyan blue symbols: Real part of the dielectric constant $\varepsilon_b(T)$ measured by dielectric spectroscopy at 45 MHz and 96.8 kHz, respectively. Red dots: Oscillator strength $\Delta\varepsilon_1$ of the lowest A_u mode. Red crosses: Sum of the oscillator strengths $\Delta\varepsilon = \sum_i \Delta\varepsilon_i$ of all A_u modes. All data sets are normalized to their value at 13 K.

$6 \cdot 10^2 \text{ cm}^{-2}$, see Fig. 13. Note that this corresponds to only 0.5% of $\omega_{p,1}^2$. Together, the decrease of $\omega_{p,1}^2$ and the increase of $\omega_{0,1}^2$ between 13 K and 10 K yield a reduction of the oscillator strength $\Delta\varepsilon_1$ of about 0.03 (see top panel of Fig. 13 and red dots in Fig. 14). Note that the sum of the changes of all other modes including the change of ε_∞ is about an order of magnitude smaller.

In the following, we estimate the oscillator strength of a possible electromagnon by comparing the results of our phonon study with the temperature dependence of the real part $\text{Re}\{\varepsilon_b\}$ measured by dielectric spectroscopy

at 45 MHz and 96.8 kHz, see Fig. 14. Consider a single infrared-active oscillator with oscillator strength $\Delta\varepsilon_i$, eigenfrequency $\omega_{0,i}$, and damping constant $\gamma_i \ll \omega_i$. For $\omega \ll \omega_{0,i}$, this oscillator gives rise to a constant contribution $\Delta\varepsilon_i = (\omega_{p,i}/\omega_{0,i})^2$ to $\text{Re}\{\varepsilon(\omega)\}$ (see, e.g., Eq. 5). For frequencies far below the phonon range, the contribution of phonons and higher-lying excitations to $\text{Re}\{\varepsilon_b\}$ may thus be approximated by $\text{Re}\{\varepsilon_b^{\text{high}}\} = \varepsilon_{yy}^\infty + \sum_{i=1}^7 \Delta\varepsilon_i$, where the sum is running over the seven A_u modes. If $\text{Re}\{\varepsilon_b^{\text{high}}\}$ is smaller than the quasi-static value of $\text{Re}\{\varepsilon_b\}$, this implies a finite contribution of a further infrared-active oscillator at intermediate frequencies. We have chosen to measure $\text{Re}\{\varepsilon_b\}$ at 45 MHz and 96.8 kHz for two reasons. First, these frequencies are far below the eigenfrequency $\omega_{0,\text{em}} \approx 2-3 \text{ cm}^{-1}$ of a possible electromagnon as observed in inelastic neutron scattering^{75,76} and terahertz spectroscopy.⁷⁷ Secondly, they are high enough to neglect contributions from domain-wall dynamics.⁷⁸ Therefore, differences between $\text{Re}\{\varepsilon_b(45 \text{ MHz})\}$ and the value of $\text{Re}\{\varepsilon_b^{\text{high}}\}$ determined from the phonon parameters have to be attributed to the possible contribution of an electromagnon.

In Fig. 14, we normalized both $\text{Re}\{\varepsilon_b(45 \text{ MHz})\}$ and $\text{Re}\{\varepsilon_b^{\text{high}}\}$ to their respective values at 13 K in order to eliminate uncertainties of the absolute value. At $T_{N1} \approx 6.5 - 8.0 \text{ K}$ the low-frequency data show a jump of $\text{Re}\{\varepsilon_b\}$ of about 0.01, in agreement with the results of Refs. [8] and [9]. The peak in the vicinity of T_{N2} reflects the washed-out divergence of $\text{Re}\{\varepsilon_b\}$ at the phase transition. Between 13 K and 10 K, $\text{Re}\{\varepsilon_b\}$ *decreases* by about 0.01. At first sight, this may seem to contradict the expected gain of oscillator strength of the electromagnon upon entering the multiferroic phase. The expected increase of $\text{Re}\{\varepsilon_b\}$ can be reconciled with the observed decrease of $\text{Re}\{\varepsilon_b\}$ by considering a decrease of the effective ionic charge causing a decrease of $\text{Re}\{\varepsilon_b^{\text{high}}\}$. As discussed above, we find that $\text{Re}\{\varepsilon_b^{\text{high}}\}$ decreases by about 0.03 between 13 K and 10 K. It is tempting to attribute the difference of 0.02 between the changes of $\text{Re}\{\varepsilon_b^{\text{high}}\}$ and $\text{Re}\{\varepsilon_b\}$ to the oscillator strength $\Delta\varepsilon_{\text{em}}$ of a possible electromagnon. However, the subtle change of $\text{Re}\{\varepsilon_b^{\text{high}}\}$ is difficult to quantify experimentally. Hence we rather interpret this value as a rough estimate for the upper boundary of the electromagnon oscillator strength, $\Delta\varepsilon_{\text{em}} \lesssim 0.02$. Using the eigenfrequency $\omega_{0,\text{em}} \approx 2-3 \text{ cm}^{-1}$ of a possible electromagnon as observed in inelastic neutron scattering and terahertz transmittance,⁷⁵⁻⁷⁷ we arrive at an estimate for the upper boundary of the electromagnon spectral weight $\omega_{p,\text{em}}^2 \lesssim 0.1-0.2 \text{ cm}^{-2}$. This value is tiny, it is about 6 orders of magnitude smaller than the oscillator strength $\omega_{p,1}^2$ of the lowest A_u phonon mode, and still more than 3 orders of magnitude smaller than the small reduction of $\omega_{p,1}^2$ observed between 13 K and 10 K.

From the point of view of symmetry, the oscillator strength of the electromagnon has to be finite in the multiferroic phase. However, symmetry does not quantify

the oscillator strength, it may be very small and hard to detect experimentally. In this context, it is interesting to note that the enhancement of the real part of the low-frequency dielectric constant $\text{Re}\{\varepsilon_b\}$ directly above T_{N2} for frequencies below about 2 GHz has been interpreted as a signature of the critical slowing down of magnetoelectric fluctuations, i.e., softening of an overdamped electromagnon.⁷⁹

We conclude that the spin-lattice interaction is not strong enough in MnWO_4 to change the phonon spectra substantially at the magnetic phase transitions. Nevertheless we are able to resolve small changes of the A_u mode lowest in energy. Note that also in the manganites AMnO_3 (with $A = \text{Gd}_{1-x}\text{Tb}_x$ and $\text{Eu}_{1-x}\text{Y}_x$) it is the phonon mode lowest in energy that is most affected by the transition to the multiferroic phase.²⁵⁻³¹ Contrary to the conventional phonon softening observed in proper ferroelectrics, the hardening of phonons at the transition to the multiferroic phase may turn out to be a characteristic property of multiferroics.²⁶⁻²⁹

2. B_u modes

Figure 15 shows the temperature dependence of the parameters of the generalized Drude-Lorentz fit for all B_u phonon modes between 10 K and 295 K. The overall picture is very similar to the case of the A_u modes. Six of the eight B_u modes soften with increasing temperature, and the largest relative redshift between 10 K and 295 K is observed for the two modes lowest in energy. The two modes with $\omega_{0,4} = 273 \text{ cm}^{-1}$ and $\omega_{0,8} = 767 \text{ cm}^{-1}$ show an unexpected *increase* of the eigenfrequency with increasing temperature. For the highest B_u mode with $\omega_{0,8} = 767 \text{ cm}^{-1}$, we attribute this behavior to the fact that the line shape of $R_{ac}(\omega)$ is not described very well by the generalized Drude-Lorentz model, as discussed above. The deviations between fit and measured data for $R_{ac}(\omega, 30^\circ)$ at about 750 cm^{-1} [panel b) in Figs. 5 and 6] show that $\omega_{0,8}$ cannot be determined with the same precision as the eigenfrequencies of the other modes with a Lorentzian line shape.

The damping constants γ_i of all B_u modes increase with increasing temperature. Similar to the A_u modes, most B_u modes show a modest increase of less than a factor of 2, while the two modes lowest in energy show a more pronounced temperature dependence. The temperature dependence of the rotation angles θ_i is only moderate, for seven modes the value of θ_i is stable within 2° . A more detailed analysis of the rotation angles would require measurements for a larger number of polarization directions χ . Finally, the temperature dependence of the oscillator strengths $\Delta\varepsilon_i$ is somewhat larger than observed for the A_u modes. Remarkably, the mode with $\omega_{0,5} = 283 \text{ cm}^{-1}$ loses more than half of its oscillator strength between 10 K and 295 K (see also Fig. 7). As in the case of the A_u modes, this strong relative change of $\Delta\varepsilon_i$ is observed for the mode with the smallest value

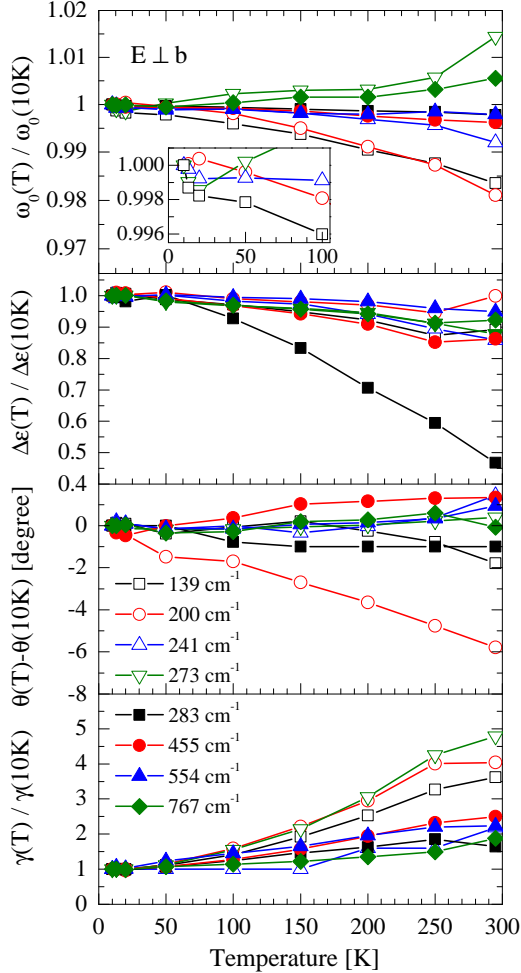


FIG. 15: (Color online) Temperature dependence of the parameters of the Drude-Lorentz fit for $E \perp b$, i.e., for the B_u phonon modes: eigenfrequency $\omega_{0,i}$, oscillator strength $\Delta\varepsilon_i$, angle θ_i , and damping γ_i . Inset: Temperature dependence of $\omega_{0,i}$ for $i \in \{1-4\}$ on an enlarged scale.

of $\Delta\varepsilon_i$.

Maczka *et al.*⁴¹ observed anomalies in the eigenfrequencies and damping constants of $\text{Mn}_{0.97}\text{Fe}_{0.03}\text{WO}_4$ and $\text{Mn}_{0.85}\text{Co}_{0.15}\text{WO}_4$ at about 50 K and around 150 to 200 K. These results were obtained from absorption measurements on polycrystalline samples, which were grown with a solvent, resulting in dark plates.⁴¹ The dark color of these samples may be caused by the dopants Fe and Co, but it may also indicate that not all Mn ions are in the divalent state, as it was found for flux-grown, undoped MnWO_4 .⁵ In our ruby-red transparent MnWO_4 crystals, we do not find any evidence for anomalies above 20 K, neither for B_u nor for A_u phonon modes.

Below 20 K, we find only subtle changes close to the experimental uncertainty. For the B_u modes, a precise determination of possible small changes of the oscillator strength $\Delta\varepsilon_i$ of oscillator i is more difficult than for the A_u modes because $\Delta\varepsilon_i$ is correlated to the value of the

orientation θ_i . The eigenfrequency $\omega_{0,1} = 139 \text{ cm}^{-1}$ of the lowest B_u mode hardens by about 0.05% between 20 K and 13 K and by about 0.13% across $T_{\text{N}2}$ between 13 K and 10 K (see the inset of Fig. 15). These values are very similar to the results obtained for the lowest A_u mode.

VI. CONCLUSION

We report on the first analysis of the full dielectric tensor in the frequency range of the phonons for any monoclinic tungstate AWO_4 with divalent A metal ions. In MnWO_4 , we unambiguously identified all infrared-active phonon modes (7 A_u modes and 8 B_u modes) and determined their temperature dependence. In particular the strongest B_u modes were overlooked in previous studies. A full polarization analysis is an essential prerequisite for the identification of the correct number of modes and of their parameters, in particular in the case of overlapping modes. For phonon modes with B_u symmetry, the combined analysis of $R_p(\omega)$ – measured with the (010) plane as plane of incidence – and $R_{ac}(\omega, \chi)$ is best suited for a reliable determination of $\hat{\varepsilon}_{ac}$ and of the phonon parameters. In the data on $R_{ac}(\omega, \chi)$ of MnWO_4 , we found deviations of the expected Lorentzian line shape around 750 cm^{-1} in a frequency range where both $\text{Re}\{\varepsilon_{xx}\}$ and $\text{Re}\{\varepsilon_{zz}\}$ are close to zero. We derived a Kramers-Kronig-consistent oscillator model which is able to describe asymmetric line shapes in compounds with monoclinic symmetry. In particular, our model also describes modes showing a gradual rise of $\text{Im}\{\varepsilon(\omega)\}$ at the low-frequency side and a steep drop at high energies. We propose that the asymmetric line shape observed in $R_{ac}(\omega, \chi)$ for near-normal incidence is caused by the mixing of longitudinal and transverse modes in a frequency range where $\text{Re}\{\varepsilon_{ac}\} \approx 0$ for all directions within the ac plane.

Based on a generalized Drude-Lorentz model, we determined the temperature dependence of the phonon parameters, including the orientation of the B_u modes within the ac plane. The phonons show only subtle changes at the magnetic phase transitions between the AF2, AF3, and the paramagnetic phase. In particular, the eigenfrequency of the lowest A_u mode *increases* by roughly 0.1% upon cooling from 13 K to 10 K, while the spectral weight decreases by $(\Delta\omega_{p,1}/\omega_{p,1})^2 \approx 0.5\%$. A comparison to the data for the quasi-static dielectric constant $\text{Re}\{\varepsilon_b\}$ yields an upper boundary for the spectral weight of a possible electromagnon of less than 0.1% of the small change $\Delta\omega_{p,1}^2$ of the spectral weight of the lowest A_u mode. Phonon hardening upon entering the multiferroic phase may turn out to be a characteristic property of magnetoelectric multiferroics of spin-spiral type. In contrast to previous reports on MnWO_4 or slightly doped $\text{Mn}_{1-x}\text{A}_x\text{WO}_4$, we do not find any anomalies above 20 K. We conclude that spin-lattice coupling in MnWO_4 is only small.

The quantitative understanding of the phonon modes

obtained here provides an excellent starting point for the analysis of the optical data of nanocrystals^{46–48} as well as for an attempt to comprehend the anomalies reported for doped polycrystalline samples.^{41,42}

It is a pleasure to acknowledge fruitful discussions with P.H.M. van Loosdrecht. This work was supported by the DFG via SFB 608.

- ¹ D. Errandonea and F.J. Manjoń, *Prog. Mater. Sci.* **53**, 711 (2008), and references therein.
- ² P. Meunier, M. Bravin, M. Bruckmayer, S. Giordano, M. Loidl, O. Meier, F. Pröbst, W. Seidel, M. Sisti, L. Stodolsky, S. Uchaikin, and L. Zerle, *Appl. Phys. Lett.* **75**, 1335 (1999).
- ³ J.-H. Zhao, T. Liu, S.-S. Guo, J. Guan, and X.-L. Wang, *Opt. Express* **18**, 18989 (2010).
- ⁴ W. Chen, Y. Inagawa, T. Omatsu, M. Tateda, N. Takeuchi, and Y. Usuki, *Opt. Commun.* **194**, 401 (2001).
- ⁵ P. Becker, L. Bohatý, H.J. Eichler, H. Rhee, and A.A. Kaminskii, *Laser Phys. Lett.* **4**, 884 (2007).
- ⁶ G. Huang, C. Zhang, and Y. Zhu, *J. Alloy. Comp.* **432**, 269 (2007).
- ⁷ O. Heyer, N. Hollmann, I. Klassen, S. Jodlauk, L. Bohatý, P. Becker, J.A. Mydosh, T. Lorenz, and D. Khomskii, *J. Phys.: Condens. Matter* **18**, L471 (2006).
- ⁸ K. Taniguchi, N. Abe, T. Takenobu, Y. Iwasa, and T. Arima, *Phys. Rev. Lett.* **97**, 097203 (2006).
- ⁹ A.H. Arkenbout, T.T.M. Palstra, T. Siegrist, and T. Kimura, *Phys. Rev. B* **74**, 184431 (2006).
- ¹⁰ G. Lautenschläger, H. Weitzel, T. Vogt, R. Hock, A. Böhm, M. Bonnet, and H. Fuess, *Phys. Rev. B* **48**, 6087 (1993).
- ¹¹ H. Nojiri, S. Yoshii, M. Yasui, K. Okada, M. Matsuda, J. -S. Jung, T. Kimura, L. Santodonato, G.E. Granroth, K.A. Ross, J.P. Carlo, and B. D. Gaulin, *Phys. Rev. Lett.* **106**, 237202 (2011).
- ¹² H. Katsura, N. Nagaosa, and A.V. Balatsky, *Phys. Rev. Lett.* **95**, 057205 (2005).
- ¹³ M. Mostovoy, *Phys. Rev. Lett.* **96**, 067601 (2006).
- ¹⁴ I.A. Sergienko and E. Dagotto, *Phys. Rev. B* **73**, 094434 (2006).
- ¹⁵ I.V. Solovyev, *Phys. Rev. B* **87**, 144403 (2013).
- ¹⁶ D. Meier, M. Maringer, Th. Lottermoser, P. Becker, L. Bohatý, and M. Fiebig, *Phys. Rev. Lett.* **102**, 107202 (2009).
- ¹⁷ D. Meier, N. Leo, G. Yuan, Th. Lottermoser, M. Fiebig, P. Becker, and L. Bohatý, *Phys. Rev. B* **82**, 155112 (2010).
- ¹⁸ K. Taniguchi, N. Abe, S. Ohtani, and T. Arima, *Phys. Rev. Lett.* **102**, 147201 (2009).
- ¹⁹ T. Finger, D. Senff, K. Schmalzl, W. Schmidt, L.P. Regnault, P. Becker, L. Bohatý, and M. Braden, *Phys. Rev. B* **81**, 054430 (2010).
- ²⁰ A. Pimenov, A.A. Mukhin, V.Yu. Ivanov, V.D. Travkin, A.M. Balbashov, and A. Loidl, *Nature Phys.* **2**, 97 (2006).
- ²¹ H. Katsura, A.V. Balatsky, and N. Nagaosa, *Phys. Rev. Lett.* **98**, 027203 (2007).
- ²² R. Valdés Aguilar, M. Mostovoy, A.B. Sushkov, C.L. Zhang, Y.J. Choi, S.-W. Cheong, and H.D. Drew, *Phys. Rev. Lett.* **102**, 047203 (2009).
- ²³ T. Kubacka, J.A. Johnson, M.C. Hoffmann, C. Vicario, S. de Jong, P. Beaud, S. Gröbel, S.-W. Huang, L. Huber, L. Patthey, Y.-D. Chuang, J.J. Turner, G.L. Dakovski, W.-S. Lee, M.P. Minitti, W. Schlotter, R.G. Moore, C.P. Hauri, S.M. Koohpayeh, V. Scagnoli, G. Ingold, S.L. Johnson, and U. Staub, *Science* **343**, 1333 (2014).
- ²⁴ T. Yildirim, L.I. Vergara, J. Iniguez, J.L. Musfeldt, A.B. Harris, N. Rogado, R.J. Cava, F. Yen, R.P. Chaudhury, and B. Lorenz, *J. Phys.: Condens. Matter* **20**, 434214 (2008).
- ²⁵ A. Pimenov, T. Rudolf, F. Mayr, A. Loidl, A.A. Mukhin, and A.M. Balbashov, *Phys. Rev. B* **74**, 100403(R)(2006).
- ²⁶ Y. Takahashi, N. Kida, Y. Yamasaki, J. Fujioka, T. Arima, R. Shimano, S. Miyahara, M. Mochizuki, N. Furukawa, and Y. Tokura, *Phys. Rev. Lett.* **101**, 187201 (2008).
- ²⁷ M. Schmidt, Ch. Kant, T. Rudolf, F. Mayr, A.A. Mukhin, A.M. Balbashov, J. Deisenhofer, and A. Loidl, *Eur. Phys. J. B* **71**, 411 (2009).
- ²⁸ R. Schleck, R.L. Moreira, H. Sakata, and R.P.S.M. Lobo, *Phys. Rev. B* **82**, 144309 (2010).
- ²⁹ J.S. Lee, N. Kida, Y. Yamasaki, R. Shimano, and Y. Tokura, *Phys. Rev. B* **80**, 134409 (2009).
- ³⁰ R. Valdés Aguilar, A.B. Sushkov, C.L. Zhang, Y.J. Choi, S.-W. Cheong, and H.D. Drew, *Phys. Rev. B* **76**, 060404(R) (2007).
- ³¹ Y. Takahashi, Y. Yamasaki, N. Kida, Y. Kaneko, T. Arima, R. Shimano, and Y. Tokura, *Phys. Rev. B* **79**, 214431 (2009).
- ³² A.M. Shuvaev, V.D. Travkin, V.Yu. Ivanov, A.A. Mukhin, and A. Pimenov, *Phys. Rev. Lett.* **104**, 097202 (2010).
- ³³ Y. Takahashi, R. Shimano, Y. Kaneko, H. Murakawa, and Y. Tokura, *Nature Phys.* **8**, 121 (2012).
- ³⁴ A.M. Shuvaev, J. Hemberger, D. Niermann, F. Schrettle, A. Loidl, V.Yu. Ivanov, V.D. Travkin, A.A. Mukhin, and A. Pimenov, *Phys. Rev. B* **82**, 174417 (2010).
- ³⁵ R.P. Chaudhury, F. Yen, C.R. dela Cruz, B. Lorenz, Y.Q. Wang, Y.Y. Sun, and C.W. Chu, *Physica B* **403**, 1428 (2008).
- ³⁶ T. Kimura, T. Goto, H. Shintani, K. Ishizaka, T. Arima, and Y. Tokura, *Nature* **426**, 55 (2003).
- ³⁷ M.N. Iliev, M.M. Gospodinov, and A.P. Litvinchuk, *Phys. Rev. B* **80**, 212302 (2009).
- ³⁸ L. Dura, H. GIBhardt, J. Leist, P. Becker, L. Bohatý, and G. Eckold, *J. Phys.: Condens. Matter* **24**, 335901 (2012).
- ³⁹ L.H. Hoang, N.T.M. Hien, W.S. Choi, Y.S. Lee, K. Taniguchi, T. Arima, S. Yoon, X.B. Chena, and I.-S. Yang, *J. Raman Spec.* **41**, 1005 (2010).
- ⁴⁰ W.S. Choi, K. Taniguchi, S.J. Moon, S.S.A. Seo, T. Arima, H. Hoang, I.-S. Yang, T.W. Noh, and Y.S. Lee, *Phys. Rev. B* **81**, 205111 (2010).
- ⁴¹ M. Maczka, M. Ptak, K. Hermanowicz, A. Majchrowski, A. Pikul, and J. Hanuza, *Phys. Rev. B* **83**, 174439 (2011).
- ⁴² M. Ptak, M. Maczka, K. Hermanowicz, A. Pikul, and J. Hanuza, *Spectrochim. Acta A* **86**, 85 (2012).
- ⁴³ I. Urcelay-Olabarria, J.L. García-Munoz, E. Ressouche, V. Skumryev, V.Yu. Ivanov, A.A. Mukhin, and A.M. Balbashov, *Phys. Rev. B* **86**, 184412 (2012).
- ⁴⁴ E.E. Koch, A. Otto, and K.L. Klierer, *Chem. Phys.* **3**, 362 (1974).
- ⁴⁵ A.B. Kuzmenko, D. van der Marel, P.J.M. van Bentum, E.A. Tishchenko, C. Presura, and A.A. Bush, *Phys. Rev.*

- B **63**, 094303 (2001).
- ⁴⁶ M. Maczka, M. Ptak, M. Kurnatowska, L. Kepinski, P. Tomaszewski, and J. Hanuza, *J. Solid State Chem.* **184**, 2446 (2011).
- ⁴⁷ M. Maczka, M. Ptak, A. Pikul, L. Kepinski, P.E. Tomaszewski, and J. Hanuza, *Vib. Spec.* **58**, 163 (2012).
- ⁴⁸ W. Tong, L. Li, W. Hu, T. Yan, X. Guan, and G. Li, *J. Phys. Chem. C* **114**, 15298 (2010).
- ⁴⁹ H. Weitzel, *Z. Kristallogr.* **144**, 238 (1976).
- ⁵⁰ J. Macavei and H. Schulz, *Z. Kristallogr.* **207**, 193 (1993).
- ⁵¹ D.L. Rousseau, R.P. Bauman, S.P.S. Porto, *J. Raman Spectrosc.* **10**, 253 (1981).
- ⁵² R. Valdés Aguilar, A.B. Sushkov, S. Park, S.-W. Cheong, and H.D. Drew, *Phys. Rev. B* **74**, 184404 (2006).
- ⁵³ A.B. Kuzmenko, E.A. Tishchenko, and V.G. Orlov, *J. Phys.: Condens. Matter* **8**, 6199 (1996).
- ⁵⁴ A.B. Kuzmenko, *Rev. Sci. Instr.* **76**, 083108 (2005).
- ⁵⁵ A. Gössling, T. Möller, W.-D. Stein, P. Becker, L. Bohatý, and M. Grüninger, *Phys. Status Solidi B* **242**, R85 (2005).
- ⁵⁶ A.S. Chaves and S.P.S. Porto, *Solid State Comm.* **13**, 865 (1973).
- ⁵⁷ D.W. Berreman and F.C. Unterwald, *Phys. Rev.* **174**, 791 (1968).
- ⁵⁸ R.P. Lowndes, *Phys. Rev.* **1**, 2754 (1970).
- ⁵⁹ A.S. Barker and J.J. Hopfield, *Phys. Rev.* **135**, A 1732 (1964).
- ⁶⁰ J. Humlíček, R. Henn and M. Cardona, *Phys. Rev. B* **61**, 14554 (2000).
- ⁶¹ T. Möller, I. Bernst, D. Panoglou, D. Muders, V. Ossenkopf, M. Röllig, and P. Schilke, *Astronomy & Astrophys.* **549**, A21 (2013).
- ⁶² A.B. Kuzmenko, E.A. Tishchenko, and A.S. Krechetov, *Opt. Spectrosc.* **84**, 402 (1998), arXiv:cond-mat/9707106.
- ⁶³ R. Lacomba-Perales, D. Errandonea, D. Martínez-García, P. Rodríguez-Hernández, S. Radescu, A. Mujica, A. Muñoz, J.C. Chervin, and A. Polian, *Phys. Rev. B* **79**, 094105 (2009).
- ⁶⁴ M. Daturi, G. Busca, M.M. Borel, A. Leclaire, and P. Pignaggio, *J. Phys. Chem. B* **101**, 4358 (1997).
- ⁶⁵ A. Kuzmin, A. Kalinko, and R.A. Evarestov, *Cent. Eur. J. Phys.* **9**, 502 (2011).
- ⁶⁶ J. Ruiz-Fuertes, S. Lopez-Moreno, D. Errandonea, J. Pellicer-Porres, R. Lacomba-Perales, A. Segura, P. Rodríguez-Hernández, A. Muñoz, A.H. Romero, and J. Gonzalez, *J. Appl. Phys.* **107**, 083506 (2010).
- ⁶⁷ L.J. Burcham and I.E. Wachs, *Spectrochim. Acta A* **54**, 1355 (1998).
- ⁶⁸ A. Damascelli, D. van der Marel, M. Grüninger, C. Presura, T.T.M. Palstra, J. Jegoudez, and A. Revcolevschi, *Phys. Rev. Lett.* **81**, 918 (1998).
- ⁶⁹ V. Ivanovski, T.G. Mayerhöfer, and J. Popp, *Vib. Spec.* **44**, 369 (2007).
- ⁷⁰ W. Baltensperger and J.S. Helman, *Helv. Phys. Acta* **41**, 668 (1968).
- ⁷¹ D.J. Lockwood and M.G. Cottam, *J. Appl. Phys.* **64**, 5876 (1988).
- ⁷² A.B. Sushkov, O. Tchernyshyov, W. Ratcliff II, S.W. Cheong, and H.D. Drew, *Phys. Rev. Lett.* **94**, 137202 (2005).
- ⁷³ C.J. Fennie and K.M. Rabe, *Phys. Rev. Lett.* **96**, 205505 (2006).
- ⁷⁴ T. Rudolf, Ch. Kant, F. Mayr, J. Hemberger, V. Tsurkan, and A. Loidl, *Phys. Rev. B* **76**, 174307 (2007).
- ⁷⁵ D. Senff, T. Finger, M. Braden, private communication.
- ⁷⁶ F. Ye, R.S. Fishman, J.A. Fernandez-Baca, A.A. Podlesnyak, G. Ehlers, H.A. Mook, Y. Wang, B. Lorenz, and C.W. Chu, *Phys. Rev. B* **83**, 140401(R) (2011).
- ⁷⁷ A. Pimenov, private communication.
- ⁷⁸ D. Niermann, C.P. Grams, M. Schalenbach, P. Becker, L. Bohatý, J. Stein, M. Braden, and J. Hemberger, *Phys. Rev. B* **89**, 134412 (2014).
- ⁷⁹ D. Niermann, C.P. Grams, P. Becker, L. Bohatý, H. Schenck, and J. Hemberger, arXiv:1408.1557.